12-2013

Quantum Dot Enhanced Epitaxial Lift-Off Solar Cells

Mitchell F. Bennett

Quantum Dot Enhanced Epitaxial Lift-Off Solar Cells

by

Mitchell F. Bennett

A Thesis Submitted
in Partial Fulfillment
of the Requirements for the Degree of
Master of Science
in Materials Science & Engineering

Approved by:

Dr. Seth M. Hubbard, Associate Professor
Thesis Advisor, Department of Physics and Microsystems Engineering

---

Dr. John Andersen, Professor
Committee Member, Department of Physics

Dr. Michael Jackson, Associate Professor
Committee Member, Department of Electrical & Microelectronic Engineering

---

Dr. Paul Craig, Professor
Department Head, School of Chemistry and Materials Science & Engineering

Department of Materials Science & Engineering
College of Science
Rochester Institute of Technology
Rochester, New York
December 2013

Thesis Release Permission Form

Rochester Institute of Technology
College Of Science

Title:

Quantum Dot Enhanced Epitaxial Lift-Off Solar Cells

I, Mitchell F. Bennett, hereby grant permission to the Wallace Memorial Library to reproduce my thesis in whole or part.

Mitchell F. Bennett

Date

Dedication

To my family, especially all loved ones that are now gone.

Acknowledgments

There are many people who I would like to thank, and many that I must:

- Dr. Seth Hubbard, for taking me on as an undergrad and allowing me to develop my researching skills in NPRL
- My committee: Drs. John Andersen and Michael Jackson
- Dr. David Forbes for his growth knowledge and fantastic karaoke skills
- Rao Tatavarti and MicroLink Devices, Inc. for ELO fabrication and processing
- Phil Ahrenkiel for TEM measurements and discussion
- NPRL Ph.D candidates: Zachary Bittner and "The" Stephen Polly for HRXRD testing assistance, MATLAB assistance, and many, many fruitful discussions; as well as Michael Slocum and Yushuai Dai for extensive PV and fish knowledge
- NPRL masters student Adam Podell for AFM and PL testing assistance, many discussions on music and cubical comic relief
- Former NPRL post-doc Chris Kerestes for MATLAB work with reflectivity simulations; current post-doc Staffan Hellström for various simulation help and discussion
- Elisabeth McClure for contact via mask design and for dealing with being my first ever minion
- John Hatakeyama for LIV testing assistance
- The NASA Small Business Technology Transfer (STTR) program for financial support under grant # NNX45CG11P, with additional support provided by the National Science Foundation (DMR-0955752)

Abstract

Embedded nanostructures such as quantum dots (QDs) have been studied for many applications in solar cells including enhanced mini-band absorption in intermediate-band solar cells and current matching in multi junction cells. The major drawbacks of using such techniques to decrease intrinsic solar cell loss mechanisms are twofold: first, it is difficult to maintain partially populated states using QDs due to a quick thermal extraction of carriers; second, QDs have a weak absorption which necessitates a near-perfect control of QD growth mechanisms to carefully ensure a balance between dot size and density. One avenue for improving absorption into QDs is to utilize a thin cell with a back surface reflector in order to increase the effective optical path length (OPL) of light through the QD region, which has the potential to increase absorption into QD states. One method for the processing of thin solar cells that has been experimentally demonstrated on large 4-$6''$ wafers is epitaxial lift-off, which takes advantage of an inverted growth and a wet chemical etch of a sacrificial release layer to remove the substrate.

In this thesis, $0.25\,\mathrm{cm}^2$ InAs/GaAs QD cells were grown on $4''$ wafers, fabricated, and processed by epitaxial lift off, creating thin and flexible devices. Materials and optical characterization techniques such as atomic force microscopy and photoluminescence were used on test structures prior to and following ELO, and analysis indicated that QD optical coherence and material quality after ELO processing were preserved, although non-uniform. This was concluded to be caused by the radial thermal profile of the growth reactor, through which spatial

dependence led to local variations in QD quality and size across the $4''$ wafer, indicative of the high temperature sensitivity of QDs. Transmission electron microscopy measurements were used to investigate defects and dislocations throughout the QD device structure that would impact performance, and showed a higher concentration of defects in regions of the wafer subject to a higher temperature during growth. A similar pattern of radial dependence was observed in solar cell devices by electrical characterization. Current-voltage measurements under one-sun AM0 illumination were taken on several cells around the wafer, showing a statistical variation in solar cell device metrics dependent on wafer position. Spectral responsivity measurements show an established cavity mode pattern in sub-host bandgap wavelengths, which is discussed as an enhancement due to the thinning of the device. Integrated external quantum efficiency shows a QD contribution to the short circuit current density of $0.23\,\mathrm{mA/cm^2}$.

In addition to optical, materials, and electrical characterization, QD and baseline ELO devices were exposed to alpha radiation to gauge the effects of a harmful environment on cell performance. The QD device exhibited a remaining factor increase of 2% (absolute) in conversion efficiency over the baseline device at an end of life alpha particle fluence of $5 \times 10^9\,\alpha/\mathrm{cm^2/s}$. In addition, linear temperature coefficients for solar cell figures of merit were extracted as a function of increasing alpha fluence. At a fluence of $5 \times 10^8\,\alpha/\mathrm{cm^2/s}$, the QD device showed an efficiency temperature coefficient $0.2\,\%/^\circ\mathrm{C}$ higher (absolute) than the baseline, indicating that the inclusion of QDs could improve the radiation and temperature tolerance of solar cell devices used for space applications.

Contents

List of Tables

List of Figures

Chapter 1

Introduction

1.1 III-V PHOTOVOLTAICS IN SPACE

Solar technology is an essential path for harnessing alternative energy, as the sun provides a significant, consistent, and substantial amount of power to the earth [1]. It is among many sources for filling the growing necessity for alternative energy routes, including wind, geothermal, and water; but is able to provide power in places or situations where it may otherwise be impractical. For example, solar cells are used in space to power satellites and allow for remote exploration of the solar system [2]. The interesting properties of semiconductors make them suitable elements in the processing of solar cells. Solar cell technologies are grouped together by their generation. First generation solar technology refers to single crystal silicon devices that are at this point mature from a manufacturing standpoint, and are the most prevalent material used for solar cells because of the inexpensiveness and abundance of silicon. Second generation devices include thin film materials such as CdTe and amorphous Si, and are inexpensive but also less efficient than first generation devices. The main

focus of third generation solar is to ”push the limit” of device efficiency, and includes III-V based material systems and multijunction solar cells.

Silicon was initially investigated for space PV, and early developments in PV processing technologies made Si solar cells easily manufacturable on a large scale. In addition, Si was and is still the formidable technology for terrestrial PV for similar reasons. Si has a reasonable bandgap for many applications, and is easily passivated with SiO_2. However, there are tradeoffs in performance for Si versus other semiconducting materials. Primarily, Si is an indirect bandgap semiconductor, which necessitates not only an energy transfer from a photon but an additional momentum transfer for carrier absorption. This leads to an undesirable absorption spectra that tails off as photon energies approach the bandgap energy. Silicon has a high mobility and therefore a high diffusion length, which allows for a high collection probability with a thicker device. However, this makes Si solar cells bulky and heavy, which is impractical in a space environment: a determining factor in device deployment is the cost to weight ratio, thus lighter cells will have a higher impact in space because ultimately the overall cost is decreased. Furthermore, Si is not a radiation hard material, which is a significant disadvantage in a space environment.

The realization of epitaxial growth during the 1980’s led to the development of III-V semiconductor compounds formed from gallium, indium, arsenide, antimony, phosphide and others to use as material systems instead of the previously used group IV elements: silicon and germanium. The III-V materials have a direct bandgap, which allows for high absorption up to the band edge; a flexibility for compound tunability and

optimization; a higher radiation tolerance, which is promising in a space environment; and a higher overall absorption, which means the grown device can be much thinner and still absorb incoming photons with energies larger than the bandgap energy. The relation of several of these compounds with respect to their bandgaps and lattice constant is shown in Figure 1.1. The semiconductors used must be lattice-matched in order to epitaxially grow materials with minimized defects (*e.g.* $In_{0.48}Ga_{0.52}P$ grown on GaAs). Only a few single crystal high quality substrates are available, such as GaAs, InP, and GaSb, which limits the choices of lattice-matched materials. In this thesis, GaAs was used as a substrate material.

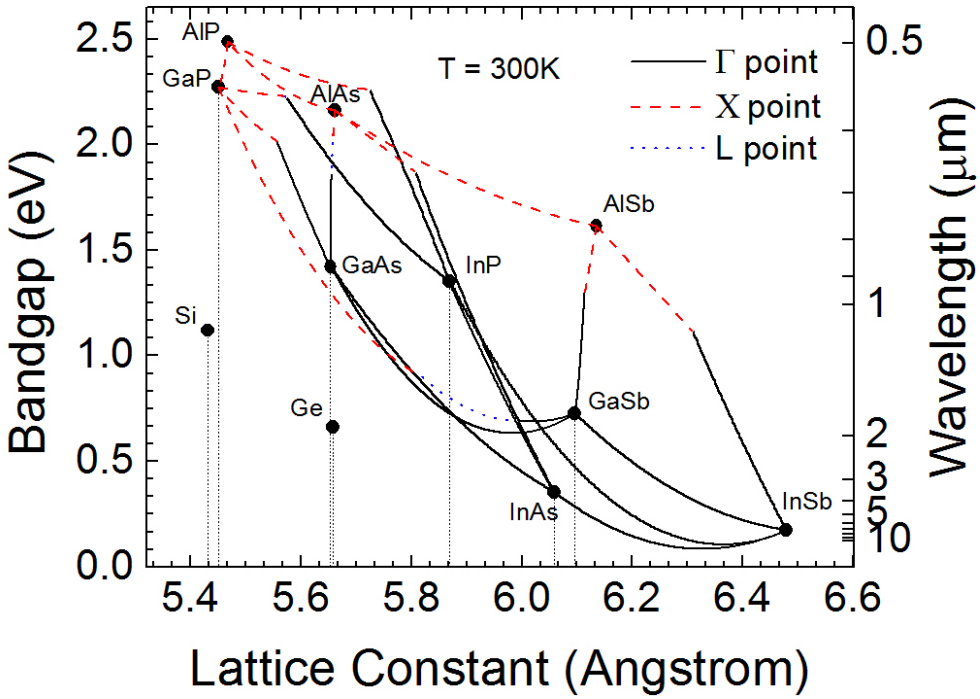

Figure 1.1: Crystal growers chart of bandgaps as a function of lattice constants at 300 K for several binary and ternary III-V semiconductors. The dotted lines aid in determining lattice-matched materials for growth. Figure courtesy of M. Slocum, RIT.

1.2 QUANTUM DOTS IN PHOTOVOLTAIC DEVICES

1.2.1 Advantage of Quantum Dot Incorporation

A rigorous model for investigating the limiting efficiencies of solar PV was established by Schockley and Queisser (SQ) in 1961 [3]. For single junction GaAs solar cells under AM0 illumination (illumination in a space environment), the theoretical upper efficiency limit calculated using this detailed balance approach is 31%. The SQ treatment attempts to quantify the significant impact of loss mechanisms to solar cells such as transmission and thermalization. Photons with energies above the bandgap of the material can be absorbed, but a photon with an energy below that of the bandgap cannot. The latter process is referred to as transmission. Photons with energies above the semiconductor bandgap generate carriers with an excess amount of energy, and relax down to the bandedge releasing that energy as heat. This mechanism is known as thermalization.

Figure 1.2 visually qualifies these intrinsic loss processes as a function of bandgap. Carnot, Boltzmann, and emission mismatches contribute some power loss realized as a reduction in either open circuit voltage or short circuit current. However, it is apparent in Figure 1.2 that the most significant impact to solar cell power loss comes from transmission and thermalization. For wide bandgap materials, thermalization is decreased but transmission losses increase. Conversely, for narrow bandgap materials transmission losses are mitigated but thermalization lends more to power loss. Clearly, there is an optimal bandgap leading to maximum power out of the cell, at 1.31 eV [4].

There have been a number of proposed techniques to overcome the SQ limit and reduce loss mechanisms. Some examples include spectrum splitting using multifunction cells and third-generation techniques such as hot carrier solar cells and impurity band absorption. These techniques to help push solar cell conversion efficiencies beyond the SQ limit can be enabled by quantum dots.

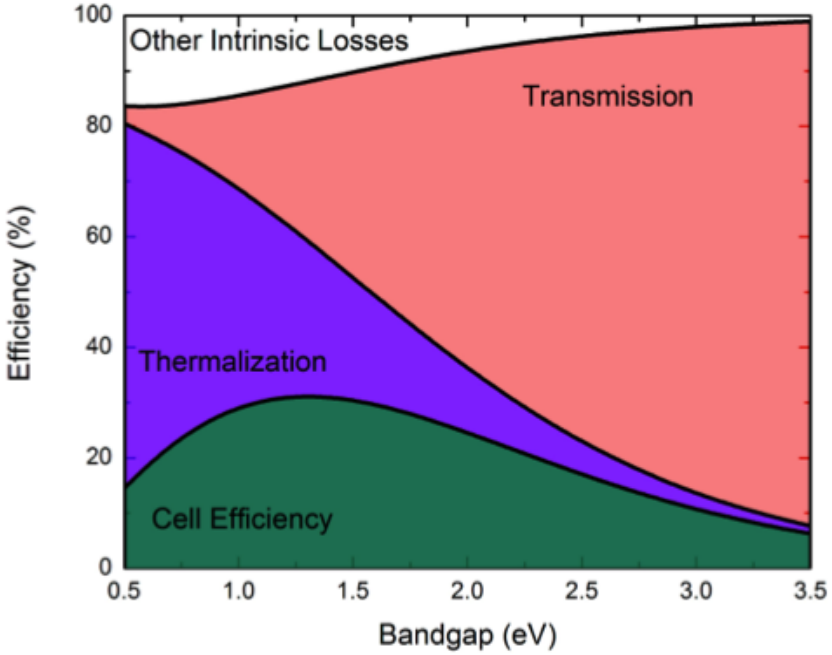

Figure 1.2: Visualization of intrinsic solar cell power loss mechanisms, such as transmission and thermalization, as a function of semiconductor bandgap. Figure courtesy of Z. Bittner, RIT.

Self-assembled strain-balanced quantum dots (QDs) have been proposed as useful candidates to enhance the absorption properties of photovoltaic solar cells in the infrared, decreasing transmission losses [5, 6, 7]. Advances in growth techniques such as metallic beam epitaxy (MBE) and metal-organic vapor-phase epitaxy (MOVPE) have made it possible to grow semiconductor nanostructures, such as QDs, on the order of several nanometers. The unique properties of quantum confined materials

contrast from ordinary bulk material behavior and establish quantized optoelectronic states. If dimensions of confinement approach and become less than the de Broglie wavelength of the carriers being confined, discrete energy levels will form in the potential well. The effects on quantum confinement in increasing dimension on the density of states (DOS) function is summarized in Figure 1.3. The DOS is a measure of the number of quantum states per unit energy. Integration of the DOS function with respect to energy will yield a total number of states, which will affect both electrical transport and optical properties of the nanostructures. QDs are quantum confined nanostructures in all three Cartesian dimensions, which leads to a discretized density of states. The optimum size of a QD is dependent on the conduction band offset, effective carrier masses, and the upper limit of the thermal population in the conduction band.

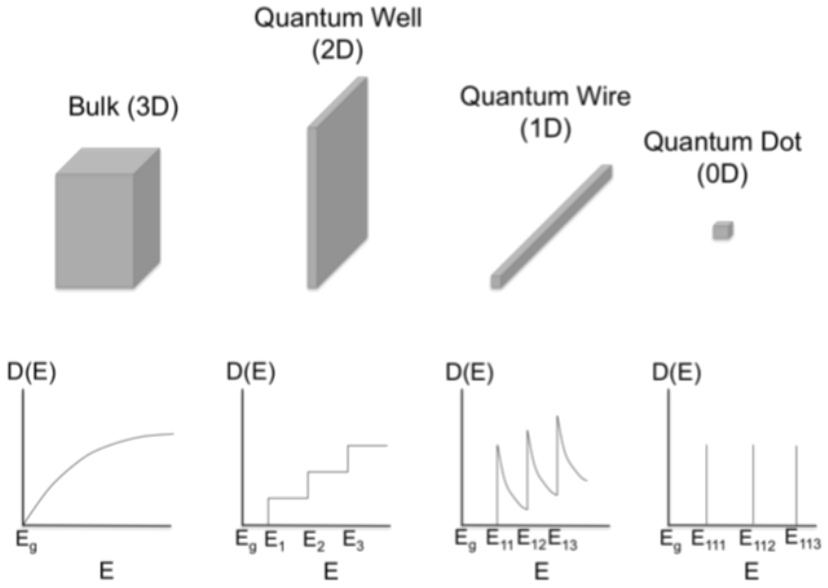

Figure 1.3: Density of states as dimensionality of confinement increases. Figure courtesy of A. Podell, RIT.

QD based solar cells include inorganic colloidal QDs and epitaxial crystalline QDs. The former are typically formed by chemical synthesis in a host matrix, and are not the focus of this thesis. Lattice mismatched materials (*e.g.* indium arsenide (InAs) on GaAs) create a certain amount of stress that is the driving force behind QD formation during epitaxial growth. The lattice constants of InAs ($6.05\,\text{Å}$) and GaAs ($5.65\,\text{Å}$) create a $7.8\,\%$ compressive mismatch. Self-assembly due to a slight lattice mismatch (2-10%) is known as Stranski-Krastanov (SK) growth. In this growth mode, monolayers are deposited epitaxially on the substrate, and the larger lattice (InAs) induces strain as the crystals compress to match the substrate below. Up to a critical thickness Θ_c, growth is 2-dimensional and forms the wetting layer (WL). After reaching Θ_c, growth follows the more energetically favorable formation of strained QD islands [8, 9]. These processes are depicted in Figure 1.4. Self-assembly using this growth regime typically results in QDs with diameters of $15-45\,\text{nm}$ and heights of $1-6\,\text{nm}$, with areal densities around $1\times10^{10}\,\text{cm}^{-2}$ [10]. This results in a relatively low dot density for a single QD layer, so multiple layers are grown to improve the overall filling factor of the superlattice, or the area filled by the QDs. However, stacking too many layers will lead to loss of material quality due to the accumulation of strain through the superlattice [11]. In order to mitigate material degradation in the superlattice, a strain-balancing technique is used to offset strain [7].

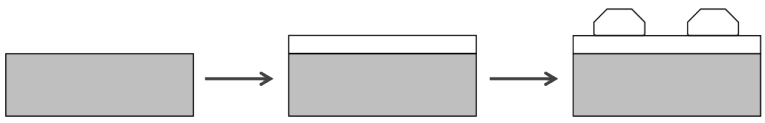

Figure 1.4: Self-assembly in the Stranski-Krastanov growth mode, through which epitaxial quantum dot growth is realized.

1.2.2 The Intermediate-Band Solar Cell (IBSC)

QDs have been investigated as an avenue for establishing mini-band absorption in intermediate-band solar cells (IBSCs) [12, 13]. This technique is potentially useful in converting sub-host-bandgap photons that would otherwise be lost to transmission: an IBSC implements a partially-filled energy band within the forbidden gap of a semiconductor, and is discussed in-depth in Refs. [14, 15]. As QDs are grown in the i-region, their wavefunctions overlap and this coupling forms a mini-band which allows for tunneling of the localized excited carriers. In an IBSC, absorption occurs from the host valence band to the intermediate band (IB), then from the intermediate band to the host conduction band as well as between the host valence and conduction bands. This technique is potentially useful in converting sub-host-bandgap photons that would otherwise be lost to transmission by allowing for multiple transitions for photon absorption with no loss in open circuit voltage. Requirements for an efficient IBSC are that the intermediate state is half-filled with electrons and favorably located so that transitions into and out of the intermediate band have equivalent absorption [16]. This is depicted in the IBSC schematic in Figure 1.5(a). Figure 1.5(b) shows a contour plot of efficiency profiles simulated using MATLAB under 1000 suns concentration. It is clear that for certain conduction band-to-intermediate band and intermediate band-to-valence band transition energy choices in an IBSC system, very high efficiencies of over 60% are theoretically attainable under concentration.

IBSCs have been investigated experimentally, although the formation of the intermediate band has proven to be a challenge. The introduction of defect levels and

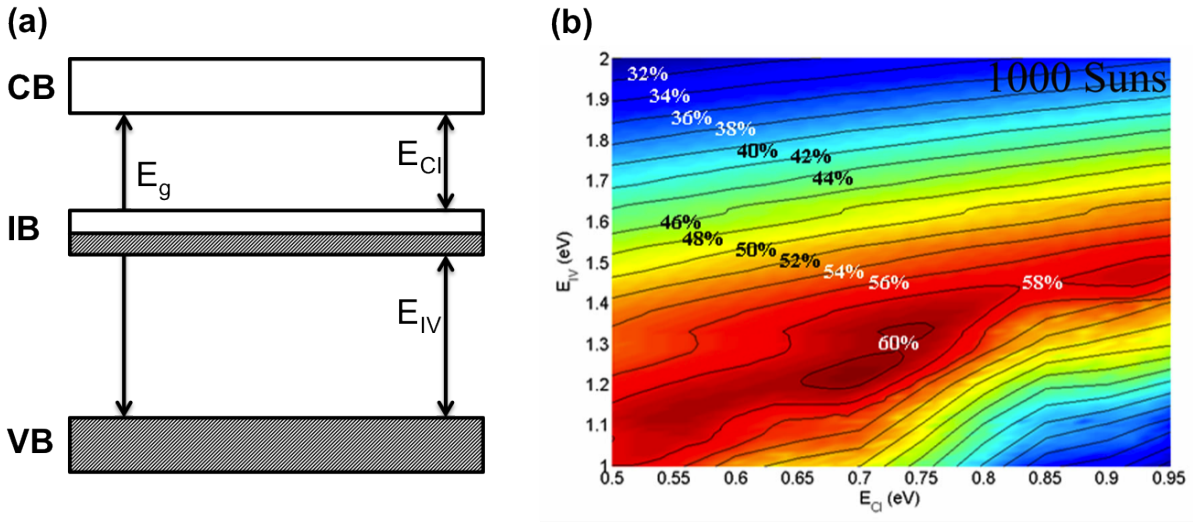

Figure 1.5: (a) IBSC diagram showing location of intermediate band (IB) in the forbidden gap in relation to the valence band (VB) and conduction band (CB); (b) MATLAB simulation showing contours for given CB-IB and IB-VB transition energies under AM 1.5 illumination at 1000 suns concentration. Figure courtesy of T. Bald, RIT.

quantum dots have been investigated to develop an IB. However, the full potential of IBSCs may be difficult to achieve due to weak absorption into quantum dots as well as the difficulty of maintaining partially populated intermediate states [17, 18]. One way to improve absorption into QD states is to improve the filling factor of the superlattice. Typically, this is achieved by growing a large number of QD layers. However, this approach will lengthen epitaxial growth time and requires optimized strain-balancing to accommodate for an increase in strain of the superlattice as more layers are added. Another way to improve absorption into QD states is to instead focus on increasing the optical path length (OPL) of light through the superlattice, which can be realized through the addition of light trapping or rear-surface light management techniques. For instance, using a highly reflective mirror on the rear surface of the solar cell can improve the reflectivity of the metal-semiconductor interface by nearly 20%, based on

calculations involving the complex indices of refraction of the materials. Although this seems like a large improvement, reflected photons will be wasted in a thick substrate due to free carrier absorption. Therefore, back surface light management necessitates the removal of the substrate. Methods to remove the substrate will be discussed in the following section.

1.3 MOTIVATION FOR THIN SOLAR CELLS VIA EPITAXIAL LIFT-OFF

Basic light events occurring in a semiconductor material are shown in Figure 1.6(a). An incoming photon can be absorbed, reflected, or transmitted through the material. In a solar cell, absorption occurs throughout the device, depending on the energy of the incoming photon. Many internal re-absorption and re-emission events, depicted in Figure 1.6(b), could potentially increase external extraction of carriers in a thin cell. The addition of a planar mirror would reflect some photons back through the device, improving their optical path length.

In order to enhance nanostructure absorption and increase the conversion efficiency of a quantum dot (QD) enhanced solar cell, the effective optical path length through the QD region must be increased. For instance, a single QD layer with density on the order of $1 \times 10^{10}\,\mathrm{cm}^{-2}$ and a height and diameter of $3\,\mathrm{nm}$ and $20\,\mathrm{nm}$, respectively, has a QD coverage in a $1\,\mathrm{cm}^2$ area of less than 15%. Growing a large number of repeated QD layers to increase the effective filling factor of the superlattice requires

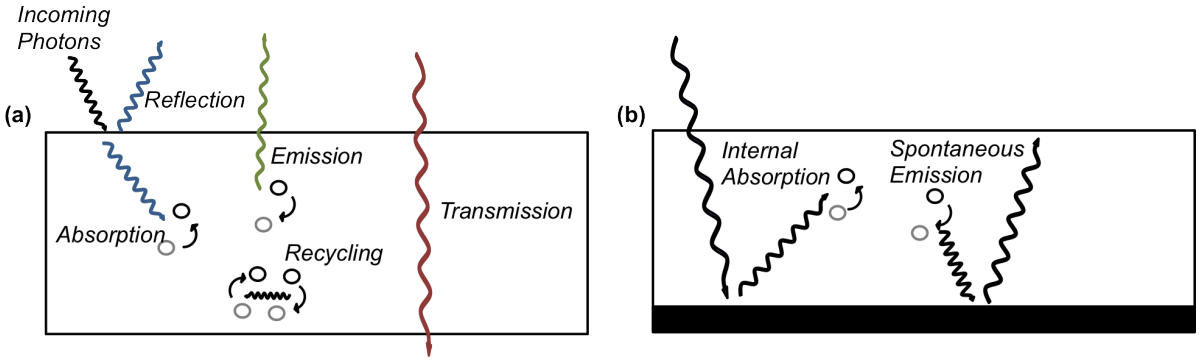

Figure 1.6: (a) Photonic events occurring in a semiconductor, including absorption, reflection, transmission, emission, and photon recycling; (b) A planar mirror on the rear surface can reflect internal photons back towards the junction or contacts for potential collection.

an extremely precise degree of strain-balancing, where slight deviations in layer thickness would result in lower open circuit voltage due to an increase in non-radiative recombination. However, the use of a backside reflector or plasmonic nanostructures in a thin film GaAs device could at least double the effective OPL of light through the active region of the device [19, 20, 21]. This effect is not seen in a traditional QDSC due to free carrier absorption in the thick substrate. Ultimately, a thin QDSC has the potential of increasing both short circuit current density and open circuit voltage: the use of a backside reflector on a thin film GaAs device will aid in reflecting bandedge and IR photons back into the device, effectively decreasing the total number of non-radiative recombination events while potentially increasing absorption into QD states. Miller and Yablonovitch argue furthermore that efficient light extraction of internal photons is necessary in minimizing non-radiative recombination and optical losses in a device [22]. Internal photons are those photons which are emitted during a recombination event, but are re-absorbed, creating a new electron-hole pair. This sequence of events can lead to total internal reflection and photon recycling, further increasing

the OPL of light in the solar cell.

Therefore, utilizing thin film QD devices allows a larger design space for nanostructure absorption enhancement. In fact, there have been many recent advances made for thin film epitaxial lift-off (ELO) GaAs devices for both single junction cells [23, 24] and multijunction systems that benefit from a cost savings due to successful substrate reuse [25, 26, 27, 28]. In addition, ELO allows for device processing on both sides of the cell to optimize current absorption and collection using mirrors or bifacial contacts [29]. Furthermore, plasmonic nanoparticles have been incorporated as light trapping structures in a single junction QD-enhanced solar cell to improve infrared photoresponse [30]. In this thesis, thin-film QD-enhanced single-junction solar cells have been grown and processed by ELO rather than the bond-and-transfer technique that has been previously reported by Tanabe et al. [31]. The ELO process in regards to this work will be discussed in detail.

1.4 RADIATION DAMAGE IN GALLIUM ARSENIDE SOLAR CELLS

Longtime goals of PV research and development have been to further increase efficiency and mass specific power while lowering cost and maintaining cell longevity. This is most important for devices grown for space applications where harmful electron and proton radiation can have a detrimental effect on unprotected cells. The next generation of space PV is the inverted metamorphic (IMM) triple junction solar cell (TJSC) [32]. The current state-of-the-art III-V upright TJSC features a top $InGaP_2$

subcell and a middle (In)GaAs subcell grown lattice matched to a Ge substrate, resulting in band gaps of 1.85 eV / 1.42 eV / 0.66 eV with a low defect density. Metamorphic, or lattice mismatched growth, allows for a larger flexibility in solar cell design: the design space created by moving toward IMM devices allows for a more optimal selection of material band gaps.

During IMM growth, each subcell is grown in a reverse order, starting with higher band gap materials. These are grown lattice matched to a GaAs substrate and include a transparent metamorphic grade to the bottom 1.0 eV subcell, which has been shown to yield conversion efficiencies of over 40% under concentrated AM1.5 spectrum [33]. If grown upright, the bottom subcell would not be lattice matched, and thus would result in a defect-ridden device. Using the inverted method, material quality can be maintained throughout all junctions. After growth, the substrate is removed, yielding a low-weight cell. High quality material growth and excellent device characteristics have been previously reported [33, 34]. Despite the noticeable advantages of these structures in a space environment, some of the IMM junctions are not as tolerant to radiation as the current upright TJSC, although improvements have been made [35, 36].

One way to improve radiation tolerance is to use quantum dots (QDs), which have been shown to be more tolerant to both electron and proton irradiation [37]. Previous studies have shown QDs to have a greater radiation tolerance than other nanostructures such as quantum wells due to the effects of 3D quantum confinement [38]. In addition, embedded QDs in the middle junction of an InGaP/(In)GaAs/Ge TJSC have

resulted in an overall better radiation tolerance to open circuit voltage degradation than similar TJSCs without QDs [39]. This can be extended to IMM devices in future work to provide a more suitable current match for the middle and bottom junctions while improving radiation hardness.

1.5 ORGANIZATION OF WORK

The following chapters describe the development and application of thin epitaxial lift-off solar cells that include an embedded superlattice of quantum dots to improve the absorption past the GaAs bandedge. There has been no previously published work on this specific process. Chapter 2 focuses on the optical, materials, and electrical characterization of these devices. This includes a detailed statistical study of several devices around a $4''$ wafer as well as a discussion of the best-performing cells and avenues for improvement. Chapter 3 presents data and analysis of the effects of α radiation on QD ELO devices. Chapter 4 presents an overall conclusion for this study and a discussion on future work to enhance the optical absorption in the QD states.

Chapter 2

Quantum Dot Epitaxial Lift-Off Solar Cell Characterization

2.1 THE EPITAXIAL LIFT-OFF PROCESS

2.1.1 Motivation

Recently, there has been renewed interest in combining innovative nano-scale features such as quantum-dots (QDs) with optically functional textures within the solar cell structure to improve efficiency in single junction III-V solar cells [30, 31]. Self-assembled InAs QDs in a single junction GaAs solar cell have experimentally demonstrated an absorption enhancement in the infrared [40], and could potentially increase conversion efficiency by reducing intrinsic losses due to photon transmission. Although the filling factor of a single QD layer is less than 15%, combining a thinner cell with light management techniques can increase the effective optical path length of light through the active region of the device.

Epitaxial lift-off is a developed procedure for processing thin film cells through the

chemical removal of the substrate and subsequent bonding to a metal handle. The crystallographic substrate is necessary for epitaxial growth, but once growth is completed it only adds an unnecessary weight and bulk material that does not aid in photon absorption or carrier collection. Removal of the substrate through ELO allows for both a reduction in cost due to substrate reuse and light management on the rear of the thin device to increase the optical path length of light.

2.1.2 Growth and Processing of ELO Test Structures and Devices

All samples were grown at NASA Glenn Research Center by metal-organic vapor-phase epitaxy (MOVPE) in a Veeco P125LDM chamber. In the MOVPE process, group-III precursors (tri-methyl gallium $TMGa$, try-methyl indium $TMIn$) and group-V sources (arsine AsH_3, phosphine PH_3) are flown into a reactor chamber. At an elevated temperature, atoms diffuse to the substrate, settle into a vacancy, and bind with the crystal structure at the surface. Byproducts are removed from the system. This growth method yields high quality crystalline material at low vacuum. ELO structures were grown on $4''$ GaAs ELO templates consisting of an *n*-type GaAs (100) substrate offcut 6° towards [110], with a pre-grown $Al_xGa_{1-x}As$ release layer used for lift-off and an *n*-type GaAs buffer layer. Structures were grown based on an inverted design, which was compatible with subsequent epitaxial lift-off. This means that a *p-i-n* growth stack top-down results in a *n-i-p* solar cell following ELO.

In order to characterize the effects of growing strain balanced QDs on an ELO template, test structures were grown with an embedded superlattice of 5 layers of

InAs/GaAs QDs used for optical and material characterization, as well as surface dots used to investigate statistical QD size distribution. The test structure growth design template is shown in Figure 2.1. Bulk unintentionally doped (UID) GaAs and InGaP layers were grown at a temperature of $620\,^{\circ}\mathrm{C}$. Highlighted in Figure 2.1 is the strain balancing technique used for QD growth in the intrinsic region. The QD growth is performed at a lower temperature than the bulk layers, at an InAs growth temperature of $480 - 500\,^{\circ}\mathrm{C}$). $2.0\,\mathrm{ML}$ of InAs deposition and a $4\,\mathrm{ML}$ GaP strain balancing layer were used. The strain balancing thickness was calculated for zero stress conditions assuming a QD density near $5 \times 10^{10}\,\mathrm{cm}^2$, a QD height of $2 - 3\,\mathrm{nm}$ and a wetting layer (WL) of $1\,\mathrm{nm}$, discussed in detail in Ref. [41]. The nominal repeat layer thickness is $12 - 13\,\mathrm{nm}$.

Two sets of inverted devices on ELO templates were grown and both of the design templates are also included in Figure 2.1. A baseline ELO structure with a GaAs emitter, i-region, and base of thicknesses 50, 100, and 2500 nm, respectively, was used as a reference device with no QDs. The structure included InGaP front window and back surface field layers for surface passivation and carrier transport enhancement. A QD ELO structure was also grown with an exact structure as the baseline except for the inclusion of a 10-layer superlattice of QDs in the intrinsic region, giving a total i-region thickness of 145 nm. The repeated period of the QDs was calculated and grown in the same way as the test structure. Zn and Si were used as *p*- and *n*-type dopants for bulk layers, and highly doped contact layers were formed by either Si or C. Doping levels and thickness for each layer in the design are depicted in Figure 2.1.

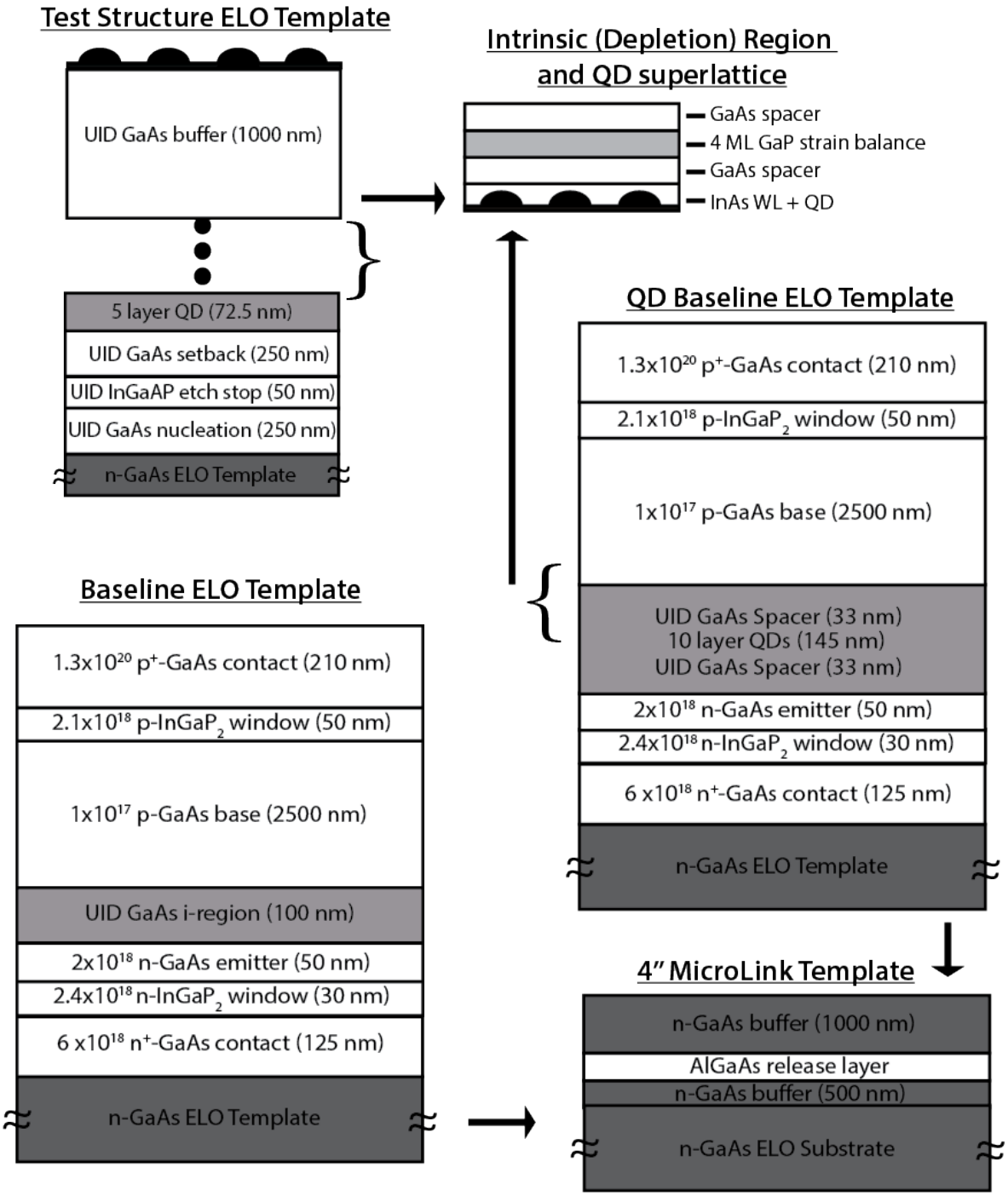

Figure 2.1: All design templates are shown above, including test structures and baseline and QD ELO device structures. Cells are flipped and polarity is reversed during the process, so the layer stacks are grown inverted. The repeated QD stack and the $4''$ ELO template are also shown.

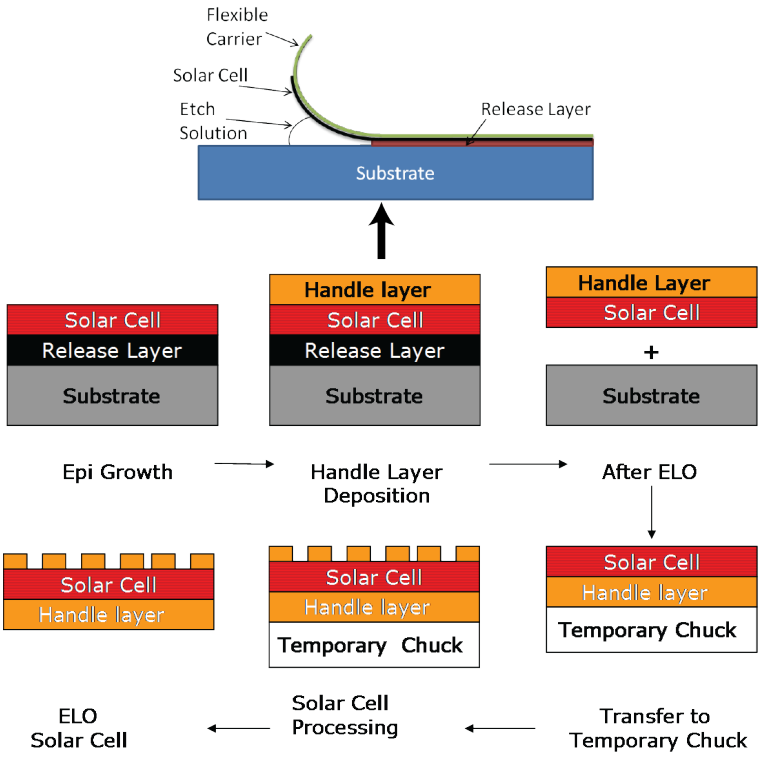

Figure 2.2: Epitaxial lift-off process flow as performed by MicroLink Devices, Inc. Device polarity is reversed during the process, so the layer stack is grown inverted. Figure courtesy of MicroLink Devices, Inc.

Epitaxial lift-off and fabrication was performed at MicroLink Devices, Inc. Specific details on the fabrication process is proprietary information and cannot be disclosed, but the ELO process is summarized as shown in Figure 2.2: following growth, a metal handle layer was applied to the top surface of the inverted solar cell structure. Next, a wafer-scale wet chemical procedure was performed to remove the solar cell and handle layer from the substrate. A thin amount of aluminum gallium arsenide ($Al_xGa_{(1-x)}As$) was used as a sacrificial release layer. An etch solution with a large selectivity between the solar cell structure and the release layer was used to remove the solar cell array on top of the $Al_xGa_{(1-x)}As$ without inducing damage to either the

solar cell or the substrate. After lift-off, the thin ELO foil was mounted to a temporary, rigid carrier for further processing, metallization, and device testing. No anti-reflection coatings were used. Figure 2.3 shows a layer design structure of the QD ELO solar cell devices pre- and post-ELO for further visual aid of the ELO process, following the ELO schematic outlined in Figure 2.2. Baseline ELO and QD ELO devices were fabricated with a 14x14 array of $0.5\text{x}0.5\,\text{cm}^2$ devices. Images of single devices are shown in Figure 2.4.

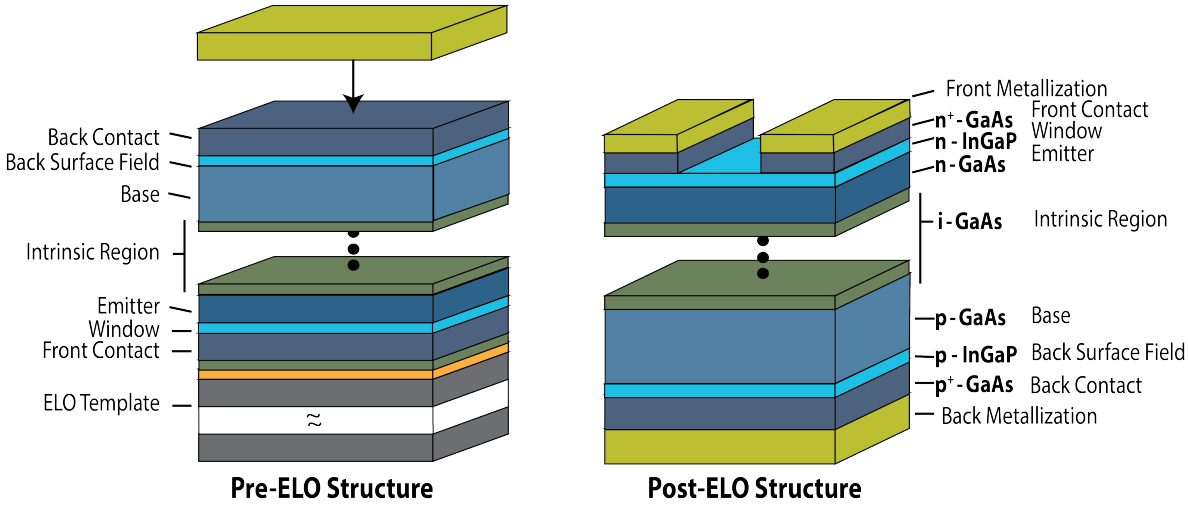

Figure 2.3: Layer structure for ELO devices pre- and post-ELO used for solar cell device characterization.

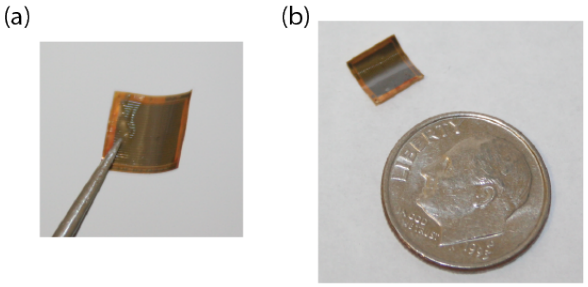

Figure 2.4: Images of a single $0.25\,\text{cm}^2$ ELO device (a), next to a US dime for reference (b).

2.2 EXPERIMENTAL SETUP

2.2.1 Basic Solar Cell Operation

A solar cell is fundamentally a *pn* junction diode. An incoming photon with energy equal to or greater than the bandgap energy of the cell will generate an electron-hole pair. Other photons are lost to transmission or indirectly transfer energy to the lattice through thermalization. A visual of the photon processes is shown on a typical band diagram in Figure 2.5.

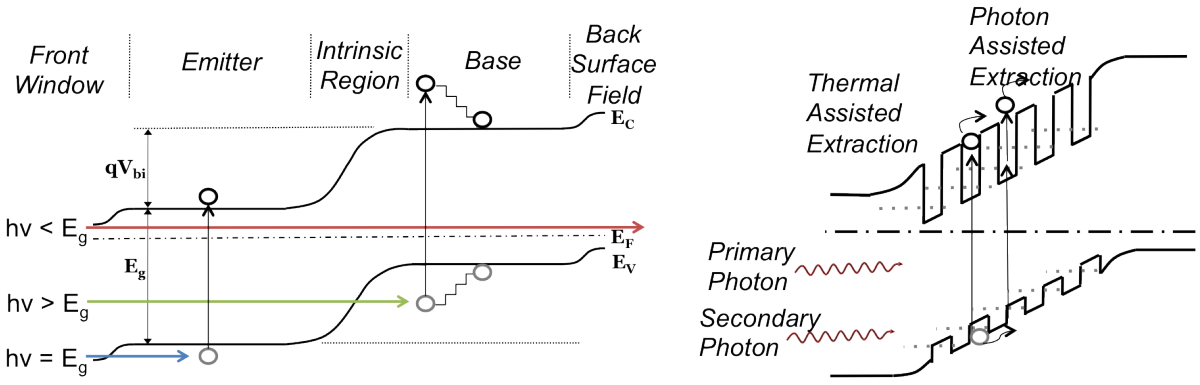

Figure 2.5: (a) *n-i-p* band structure detailing relative energies of the grown materials; (b) zoom of the intrinsic region showing a 5x layer of QDs.

An electron or hole generated due to light is known as an injected carrier, and as such is not immediately bound to the crystal lattice and is free to move, resulting in some carrier transport in addition to thermal excitation. Carrier transport comes in two forms: drift and diffusion. For an ideal diode in equilibrium, the drift and diffusion components are equal and opposite, thus there is no net current flow. Photonic excitation takes the diode out of equilibrium, resulting in additional minority carriers that diffuse toward the junction and are swept across due to the built-in electric field between the

p and *n* sides. It is assumed that a single absorbed photon with $E>E_g$ generates one electron-hole pair.

The amount of current generated at zero applied forward bias is called the short circuit current (J_{sc}). As forward bias is applied to the diode, the diode current begins to balance out the light injected current until a point is reached where there is no net current through the diode. This point is termed the open circuit voltage (V_{oc}). Thus, the total current is the light injected current minus the diode current, as shown in the the well known diode Equation 2.1. Here, J_L is the light injected current density and q and k_B are the fundamental charge and Boltzmann constant, respectively, and T is the operating temperature. J_0 is a lumped parameter called the reverse saturation current density that depends on material properties such as diffusion lengths, doping levels, and diffusivity constants, and n is the cell ideality factor. J_0 and n are used to describe cell performance and will be discussed in further detail later.

$$J = J_L - J_0\left(e^{\frac{q(V)}{nk_BT}} - 1\right) \tag{2.1}$$

The diode J-V curve is shifted into the fourth quadrant by J_{sc}, and is plotted in relation to J_L in Figure 2.6, left. This operation range is termed the "power quadrant," and by convention is flipped into the first quadrant to show power generation for the solar cell as in Figure 2.6, right. The point on the $J-V$ curve where the maximum power is generated is called P_{max}. The fill factor is calculated from P_{max} with Equation 2.2. The solar cell conversion efficiency (η) is the ratio of the maximum generated power P_{max} to the incident power P_{in} at a given illumination, or P_{max}/P_{in}. For the AM0

spectrum, P_{in} is taken to be $136\,\mathrm{mW/cm^2}$. The solar cell metrics J_{sc}, V_{oc}, P_{max}, and FF are also depicted on the right J-V curve in Figure 2.6.

$$FF = \frac{P_{max}}{I_{sc} * V_{oc}} = \frac{I_m * V_m}{I_{sc} V_{oc}} \tag{2.2}$$

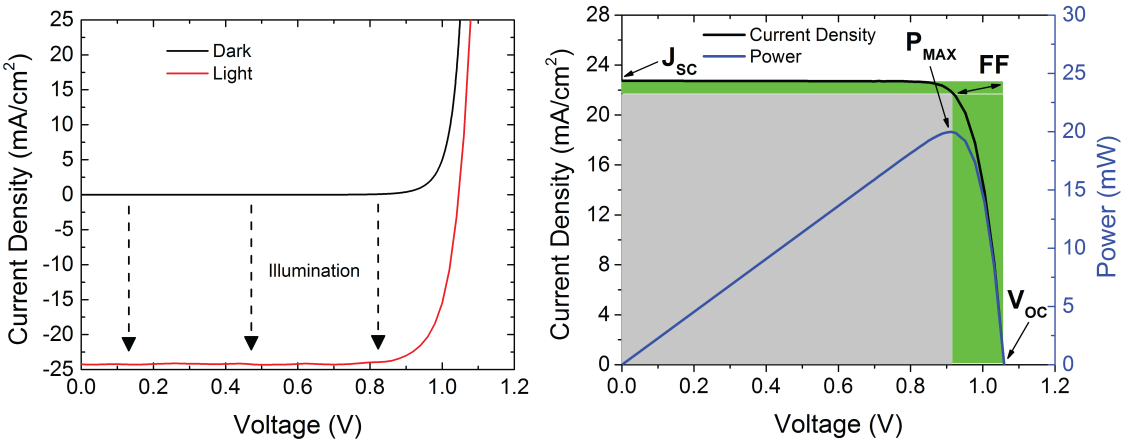

Figure 2.6: On the left, the effect of current generation due to light is shown. The light IV is typically flipped into the first quadrant, shown on the right with important solar cell figures of merit.

2.2.2 Solar Cell Testing Methodologies and Experimental Setups

Materials and optical characterization was performed via atomic force microscopy, photoluminescence, electroluminescence, high resolution X-ray diffraction, and transmission electron microscopy. The testing methods and performed experiments are outlined here. Prior to ELO, atomic force micrographs (AFM) of the test structures were taken using a Veeco Dimension 3100 AFM operating in tapping mode. The tool brings a piezoelectric tip attached to a cantilever across the wafer and measures a potential. A potential difference is measured when the tip reaches a surface structure.

Scanning across larger areas leads to an image with nanometer resolution that is used to detect surface features. Several 1x1 μm measurements were taken on each test structure to characterize QD uniformity across the 4-inch test structure. Scanning Probe Image Processor (SPIP) software was used to calculate statistically based values for QD density, height, and diameter from the AFM images [42].

Optical properties of the QDs were investigated before and after ELO using photoluminescence, taken with a 514 nm Argon ion laser and sensed with an InGaAs detector at room temperature and a Horiba Jobin iHR320 monochromator. A block diagram of the PL setup is shown in Figure 2.7. This technique utilizes a laser to pump light at a high power density to promote carrier emission.

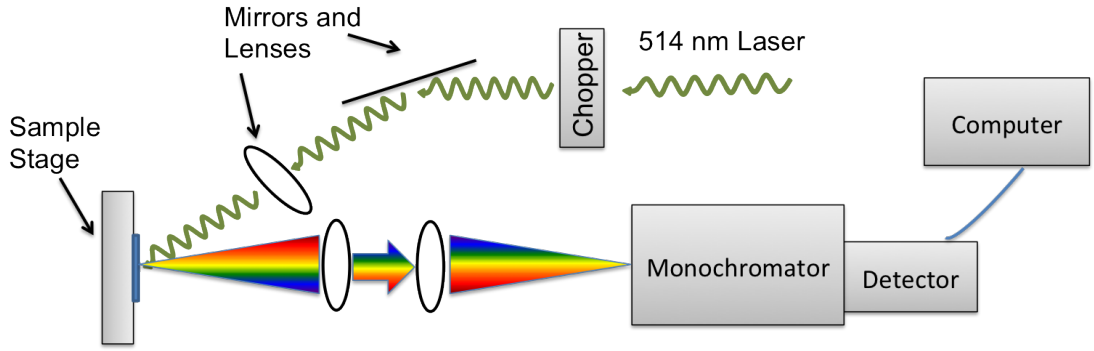

Figure 2.7: Block diagram of a photoluminescence setup.

Stimulated carriers cannot be collected electrically and recombine. This results in a high intensity luminescence at wavelengths typically corresponding to the GaAs band-to-band transition, the wetting layer transition, and the quantum dot ground state transition. Due to the smaller bandgap of the QD structures, carriers that fall into these states will recombine at a longer wavelength than the bulk GaAs material. This technique is useful in evaluating the relative intensities and peak locations for

these transitions. The statistical spread of the varying island sizes that is investigated through atomic force microscopy techniques is inherent of a QD ensemble created by self-assembly methods, and it is well known that this size distribution of the QDs leads to inhomogeneous broadening of the optical emission. This results in broad PL peaks with a full width at half maximum that is typically on the order of several tens of nanometers.

A technique similar to PL that requires an electrical bias and a complete metallization to excite carriers is called electroluminescence (EL). This measurement is useful to determine states resulting quantum-confined structures that have different bandgaps than the bulk semiconductor. A forward bias is applied to the device to increase carrier recombination and the photon emission that results is sent through a fiber optic cable and monochromator to detect and relate spectral information for the device.

A Bruker D8 Discover high-resolution X-ray diffractometer was used to measure the strain in the QD superlattice with $\omega/2\theta$ scans of the [004] plane reflections. Out-of-plane strain values of the superlattice with respect to the GaAs substrate were extracted using a differential formula for Bragg's law, given in Equation 2.3. Here, $\Delta\theta_{SL}$ is the difference in angle between the substrate Bragg peak and the zeroth order superlattice peak, θ_b is the value of the substrate Bragg angle, and $\Delta a/a$ is the fractional mismatch representing the out-of-plane strain in the superlattice.

$$\frac{\Delta a}{a} = \Delta\theta_{SL} cot\theta_b \tag{2.3}$$

Using this technique, three important figures of merit related to the superlattice strain can be extracted: one, a positive or negative value will describe if the strain is compressive or tensile. This is important in strain balancing optimization. Two, a value for strain is calculated, quantifying the amount of strain on the superlattice. Strain values are typically in the several hundreds of parts per million (ppm). Finally, the periodicity or total thickness of the superlattice can be calculated and compared to growth design.

Cross-sectional Transmission electron microscopy (TEM) measurements can be used to investigate defects and give information on the type and size of the defect as well as the location within the structure. In this technique, a beam of electrons is transmitted through a very thin sample, forming an image of interactions with the material. This is then magnified, focused, and detected by a sensor. Due to the small de Broglie wavelength of electrons, this technique has the capability of imaging at a significantly high resolution. Faults in the structure of the crystal lattice as well as the quality of the QD superlattice can be readily viewed using this technique. TEM measurements were provided by Phil Ahrenkiel at the South Dakota School of Mines and Technology.

Electrical device characterization was performed through current-voltage measurements in the dark and at 1-sun AM0 illumination, and spectral response. A useful test in characterizing diode performance described previously is through dark J-V and J_{sc}-V_{oc} measurements. Modifications to the ideal diode equation are made by taking parasitic resistances such as series (R_s) and shunting (R_{sh}) into account, resulting in

Equation 2.4. J_0 is based on material properties as well as parasitic generation resulting from interfacial states resulting from trap states and non ideal crystal growth, undesired dopants, and un-passivated side wall bonds. All of these will increase the reverse saturation current. The ideality factor, n, is used to derive assumptions related to recombination and generation relationships within the diode. An ideality factor of $n = 1$ leads to the assumption that recombination and generation occurs in bulk semiconductor outside the intrinsic region or that the device is under low-level injection. Ideality factors closer to $n = 2$ describes more recombination and generation taking place in the intrinsic region or that recombination is limited by both carrier types, an assumption resulting from high-level injection. Any change in n will affect the slope of the dark J-V curve and have a significant impact on diode performance.

$$J = J_L - J_0\left(e^{\frac{q(V-JR_s)}{nk_BT}} - 1\right) - \frac{V + JR_s}{R_{sh}} \tag{2.4}$$

J_{sc}-V_{oc} was used to extract the series resistance described above. J_{sc} and V_{oc} were measured via LabVIEW using a Keithley 2400 under increasing concentration from a quartz tungsten lamp array powered by a Sorensen DLM 80-7.5 power supply. At high currents, the dark J-V and J_{sc}-V_{oc} curves deviate from one another due to resistive losses. These losses are eliminated in the J_{sc}-V_{oc} measurement as all data is taken at conditions where no power is dissipated in the device. Comparing the currents at 1-sun was used to calculate series resistance.

Device performance characteristics under AM0 illumination were measured using a dual source solar simulator from TS Space Systems, calibrated using secondary

standards to provide a close match to 1-sun solar spectrums. Supplied $4\,\mathrm{cm}^2$ subcells from the NASA Glenn Research Center that were used in an international round robin test were used to calibrate the solar simulator [43]. A block diagram of the system is shown in Figure 2.8. A $6\,\mathrm{kW}$ hydrargyrum medium-arc iodide (HMI) lamp provides UV and visible light and a $12\,\mathrm{kW}$ quartz-tungsten-halogen (QTH) lamp provides near-IR and IR light. The complete spectra from the lamps is shaped using filters and a dichroic mirror, and a large folding mirror focuses the light down onto the device-under-test (DUT) placed on the metal chuck.

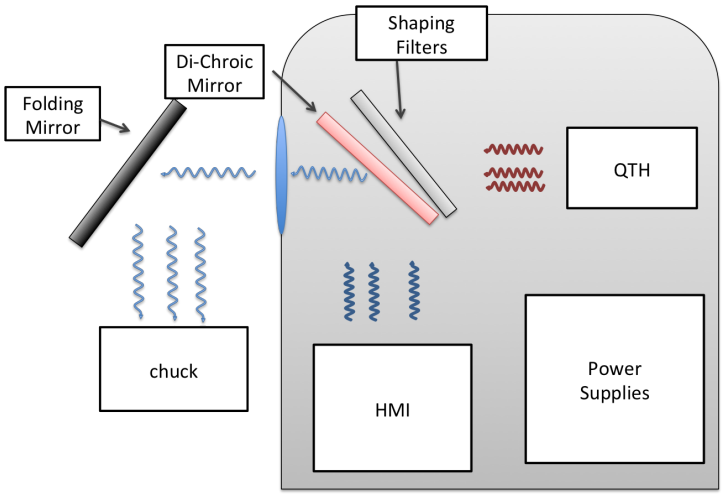

Figure 2.8: Block diagram for the TSS solar simulator showing two lamp zones and various filters used for spectral shaping and tuning.

Calibration for these tests used an InGaP subcell with a bandgap of $1.75\,\mathrm{eV}$ to calibrate the HMI followed by a GaAs subcell with a bandgap of $1.42\,\mathrm{eV}$ to set the QTH lamp voltage. A plot of the simulator intensity as well as the ASTM AM0 spectrum is shown in Figure 2.9 with the GaAs bandedge cutoff of 878 nm. A 6000K blackbody, often used to approximate the temperature of the sun, is included for reference. The

solar simulator is used to calculate various solar cell figures of merit such as the short circuit current J_{sc}, open circuit voltage V_{oc}, fill factor FF, and efficiency η, as described in the previous section.

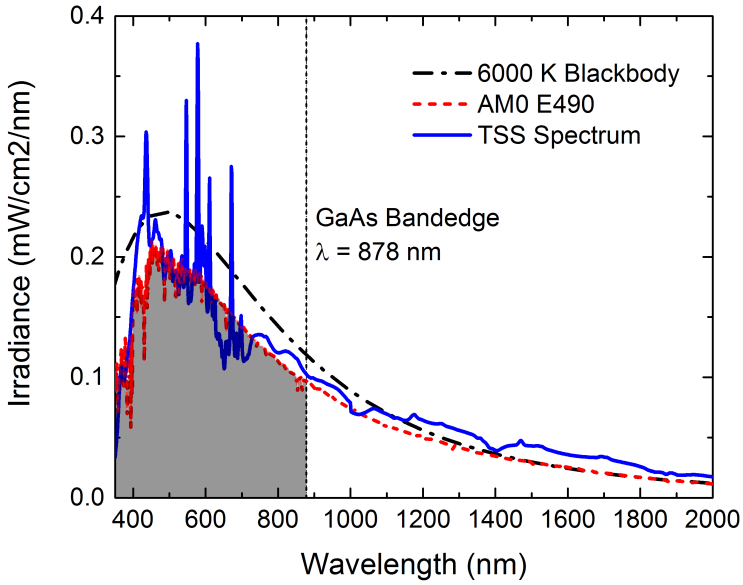

Figure 2.9: Spectra for the two zones of RIT's solar simulator overlaid on the AM0 spectrum.

Spectral responsivity measurements were taken to analyze absorptive properties of the devices using an Optronics Laboratories OL 750-S Monochromater with an OL750-HSD-300 Silicon detector that was calibrated using a Si calibration standard. A block diagram of the setup is depicted in Figure 2.10. A tungsten lamp sends light through a monochromator and chopper, and a single wavelength is optically focused down onto the sample. The sample is held at short circuit, and a current is measured. Due to the low currents typically measured, the signal is amplified using a preamplifier and lock-in amplifier before being sent to the computer system. Spectral responsivity is calculated as the ratio of this current to the input power of the lamp, and is typically

depicted as a function of wavelength. This ratio can be converted to external quantum efficiency (EQE) by Equation 2.5. EQE quantifies the absorption and collection probability of incoming photons as a function of wavelength, and provides for a normalized analysis of carrier transport throughout the cell.

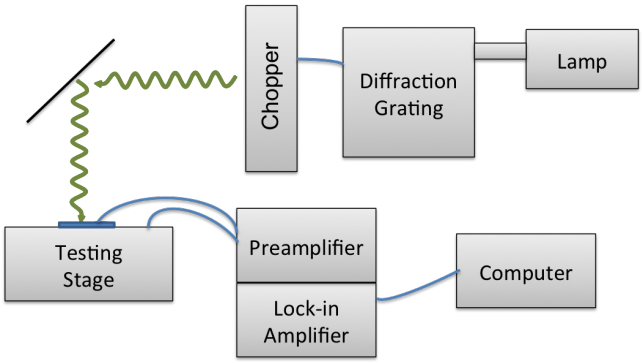

Figure 2.10: Block diagram of a spectral response setup.

$$EQE = SR * \frac{hc}{q\lambda} \tag{2.5}$$

An in-house MATLAB model was valuable in visually separating the contributions to the EQE from different regions of the cell. The model follows the work of Hovel & Woodall in the 1970's [44]. The model uses a series of carrier transport equations in conjunction with absorption data and the flux at a given wavelength, ϕ, to extract useful carrier parameters such as minority carrier diffusion lengths, surface recombination velocities, and minority carrier lifetimes. Absorptive regions of the cell include a front high-bandgap window layer, emitter, space-charge region, and base. Current generated and collected in the front window layer is described by Equation 2.6, where α_w, D, L_w, τ_w S_w are the absorption coefficient, thickness, diffusion length, lifetime,

and surface recombination velocity in the front window layer, respectively. The emitter collection is given by Equation 2.7, where α_e, d, L_e, τ_e S_e are the absorption coefficient, thickness, diffusion length, lifetime, and surface recombination velocity in the emitter material, respectively. The collection in the space-charge region is given by Equation 2.8, where the assumption in the depletion region (width W) is made that all carriers are swept out quickly by the large drift component of the electric field and hence collected. Equation 2.9 gives the base contribution to carrier collection for an assumed long-base diode with a width w and minority carrier diffusion length L_b. The total modeled spectral response of the cell is given as the summation of the previously calculated regions as in Equation 2.10. A measure of the short circuit current density is obtained by integrating the product of measured data or modeled data from Equation 2.10 across all wavelengths, as in Equation 2.11. Here, SR_λ is the spectral response of the cell and $\phi_{spec\lambda}$ is the spectrum.

$$J_D = \frac{q\phi\alpha_w L_w}{\alpha_w^2 L_w^2 - 1}\left[\frac{\alpha_w L_w + S_w\frac{\tau_w}{L_w}\left(1 - e^{-\alpha_w D}cosh\frac{D}{L_w}\right) - e^{-\alpha_w D}sinh\frac{D}{L_w}}{S_w\frac{\tau_w}{L_w}sinh\frac{D}{L_w} + cosh\frac{D}{L_w}} - \alpha_w L_w e^{-\alpha_w D}\right] \tag{2.6}$$

$$J_{D+d} = \frac{q\phi e^{-\alpha_w D}\alpha_e L_e}{\alpha_e^2 L_e^2 - 1}\left[\frac{\alpha_e L_e + S_e\frac{\tau_e}{L_e}\left(1 - e^{-\alpha_e d}cosh\frac{d}{L_e}\right) - e^{-\alpha_e d}sinh\frac{d}{L_e}}{S_e\frac{\tau_e}{L_e}sinh\frac{d}{L_e} + cosh\frac{d}{L_e}} - \alpha_e L_e e^{-\alpha_e d}\right] + \frac{J_D}{S_e\frac{\tau_e}{L_e}sinh\frac{d}{L_e} + cosh\frac{d}{L_e}} \tag{2.7}$$

$$J_W = q\phi e^{-\alpha_w D} e^{-\alpha_e d}(1 - e^{-\alpha_e W}) \tag{2.8}$$

$$J_{D+d+w} = q\phi e^{-\alpha_w D} e^{-\alpha_e d} e^{-\alpha_e W} L_b \frac{\alpha_e L_b}{\alpha_e L_b + 1} \tag{2.9}$$

$$SR(\lambda) = \frac{J_{D+d}(\lambda) + J_W(\lambda) + J_{D+d+w}(\lambda)}{q\phi(\lambda)} \tag{2.10}$$

$$J_{SR} = \int SR_\lambda \phi_{spec\lambda} d\lambda \tag{2.11}$$

2.3 CHARACTERIZATION RESULTS AND DISCUSSION

2.3.1 Materials and Optical Discussion

Initially, test structures were grown using the previously described method. The test structures included an embedded superlattice with 5 repeat units of InAs QDs used for optical and material characterization, as well as surface dots used to investigate statistical QD size distribution prior to performing ELO. Characterizing these test structures allowed for an investigation of materials and optical properties from growing strain-balanced QDs on an ELO template. Atomic force micrographs taken across the test structure are depicted in Figure 2.11 with a z-scale for reference as well as a representative 3D image. A QD height of $5\,\mathrm{nm}$ was used to filter the data through SPIP into small and large QD bins, summarized in Table 2.1. Average values

compiled from these statistics gave uniformly sized QDs with a small dot density of $2.4 \pm 0.8 \times 10^{10}\,\mathrm{cm}^{-2}$. Statistical small dot sizes observed were $2.9 \pm 0.3\,\mathrm{nm}$ in height and $17.8 \pm 2.3\,\mathrm{nm}$ in diameter. These values are similar to previously reported values [40, 45], indicating that uniform, non-coalesced QDs can be deposited on $4''$ GaAs wafers pre-grown with an AlGaAs release layer and GaAs buffer.

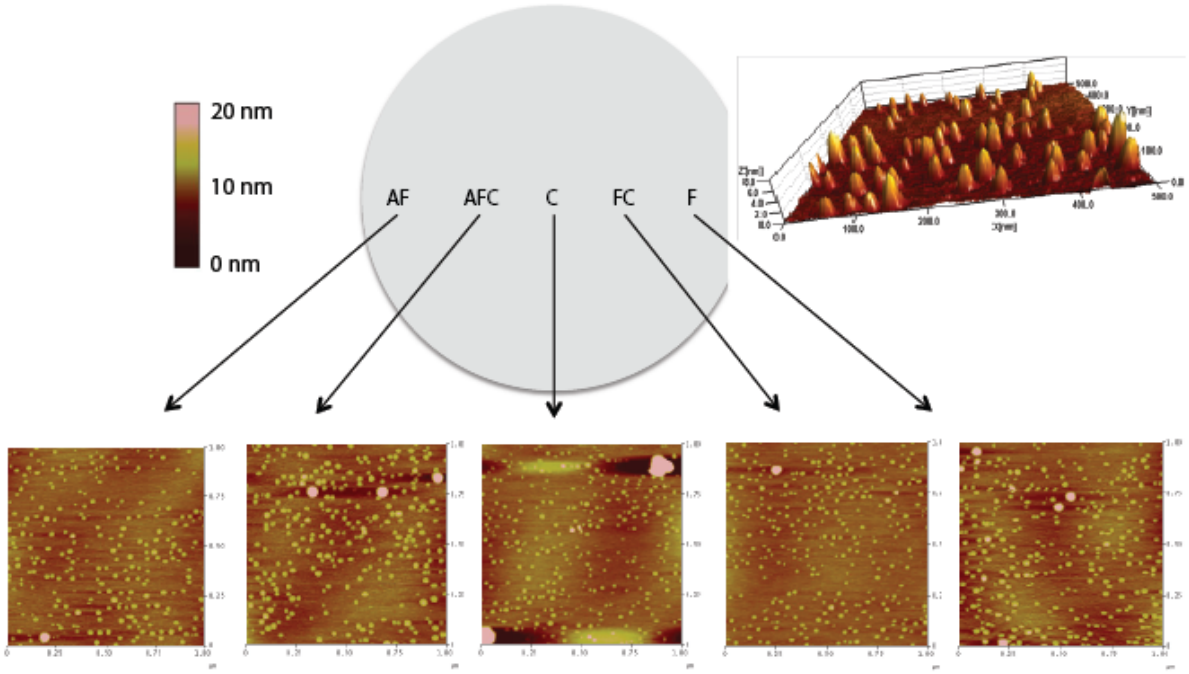

Figure 2.11: Atomic force micrographs taken at 5 points across the test structure.

Table 2.1: Atomic Force Micrograph Statistical Analysis

	Small QDs			Large QDs		
Position	Density ($\times 10^{10}\,\mathrm{cm}^{-2}$)	Height (nm)	Diameter (nm)	Density ($\times 10^{9}\,\mathrm{cm}^{-2}$)	Height (nm)	Diameter (nm)
Anti-Flat (AF)	1.0	3.2	17.1	0.7	6.6	24.3
Anti-Flat-Center (AFC)	2.8	3.0	21.6	3.2	8.1	21.7
Center (C)	2.5	2.6	15.9	3.3	16.7	22.6
Flat-Center (FC)	3.0	2.5	15.4	0.3	8.2	24.8
Flat (F)	2.9	3.1	18.9	2.4	8.0	23.0
Average	2.4	2.9	17.8	2.0	9.5	23.3
Standard Deviation	0.8	0.3	2.3	1.3	3.6	1.1

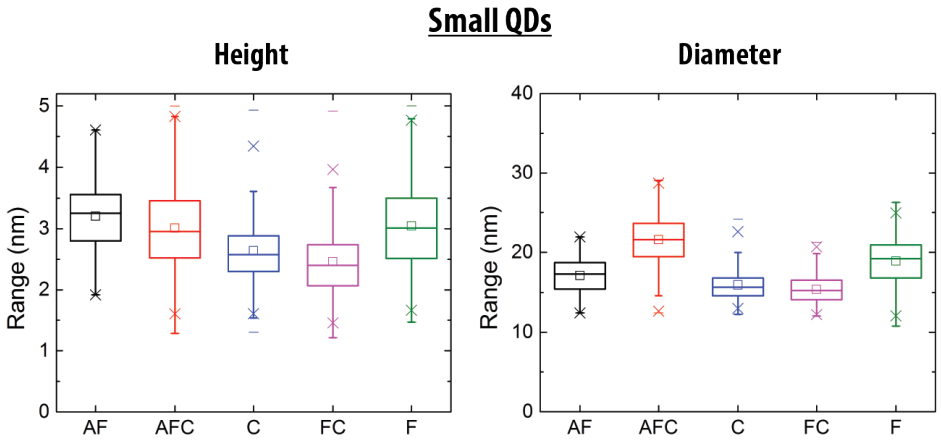

Figure 2.12: AFM statistical trends taken at 5 points across the test structure for small QDs with a height less than 5 nm.

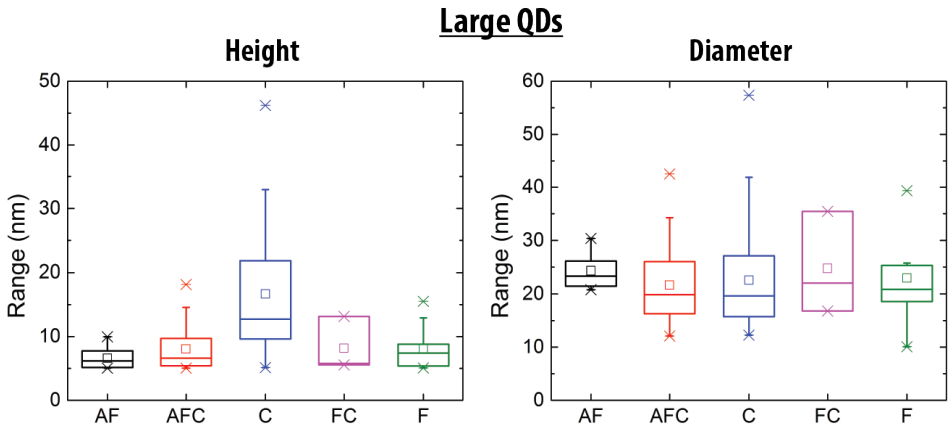

Figure 2.13: AFM statistical trends taken at 5 points across the test structure for large QDs with a height greater than 5 nm.

It is important to note the QD size trends and variations across the $4''$ test structure, as seen in Figures 2.12 and 2.13. Extracted values for density and size of small and large dots indicate that there is a local variation in QD size across the wafer. Figure 2.14 depicts growth differences for $2''$ and $4''$ wafers: the reactor can accommodate either three $2''$ wafers or a single $4''$ wafer. For the latter situation, the $4''$ wafer is

placed in the middle of the platen, such that the center of the wafer is right above the spindle used for rotation. Heat transfer to the spindle results in a variation in the thermal profile of the susceptor and platen, which is translated to the wafer. As QDs are very temperature sensitive [10, 46], QD size and quality are not constant across the larger wafer in this growth situation. The effect of this inconsistent temperature profile was also observed through optical means using photoluminescence.

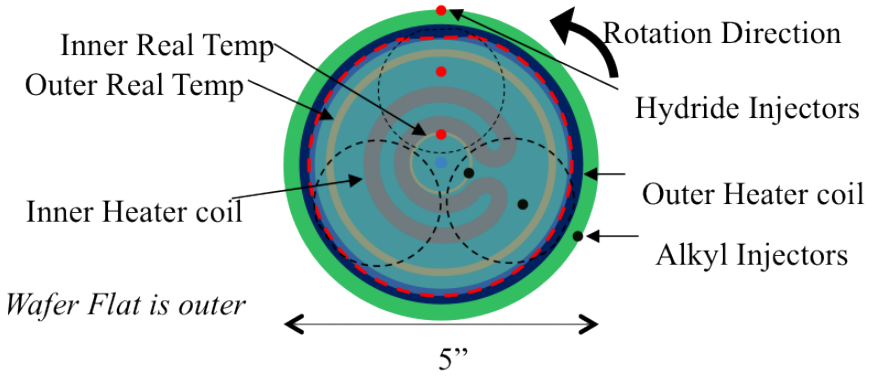

Figure 2.14: Top-down representative image of wafer placement on the platen during growth. The platen can hold up to three $2''$ wafers (black dashed lines) or a single $4''$ wafer (red dashed line).

Photoluminescence and X-ray diffraction were taken on the test structure at points corresponding to the center, flat-center, and flat locations of the wafer. AFM binned statistics for heigh and diameter for these locations as well as the PL and HRXRD measurements are shown in Figure 2.15. PL was used to investigate relative transition strengths and intensity peaks, while HRXRD was used to describe the effects of strain and strain balancing.

The PL scans depict three clear peaks which are described by an 8-band $k \cdot p$ model for InAs QDs in GaAs [47]. The emission around $875\,\mathrm{nm}$ is labeled as the GaAs substrate band-to-band transition. The other two peaks arise from sub-GaAs bandgap

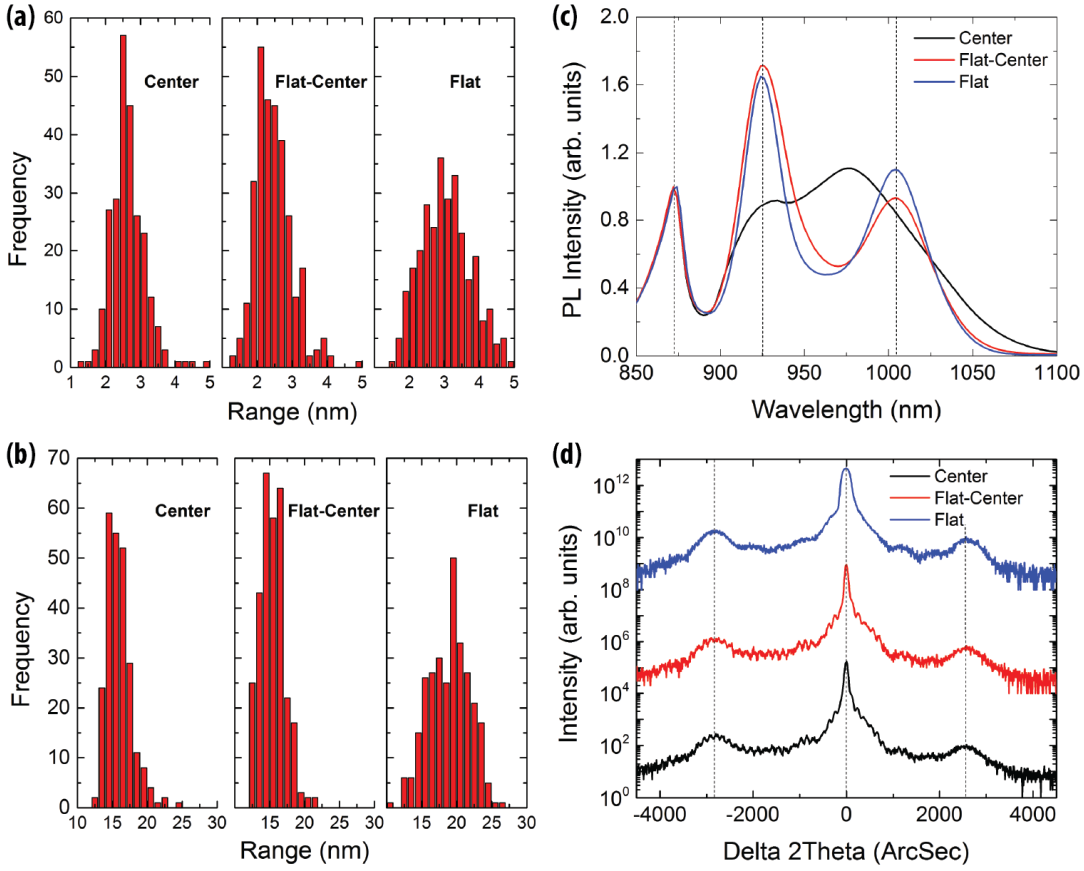

Figure 2.15: AFM binned statistics for three points showing height (a) and diameter (b) for a pre-ELO test structure radially outward from the center. These test structures additionally underwent PL (c) and HRXRD (d) measurements at similar points on the wafer.

transitions and are known as the wetting layer (WL) transition (around $925\,\mathrm{nm}$) and the ground state (GS) InAs QD transition. For the flat and center-flat scans, this value was around $1000\,\mathrm{nm}$, but a drastic blue-shift was seen in the intensity peak in the center scan. All PL peaks were fit with a Gaussian profile to study effects due to inhomogeneous broadening of the QD ensemble. Peak wavelengths and FWHM values resulting from fits are summarized in Table 2.2, along with strain and superlattice periodicity values calculated from HRXRD measurements. Superlattice periodicity is

consistent with growth design described in the previous section. Other than the center scan, FWHM values are low and have similar peak wavelength values. For the center scan, there is a drastic broadening of both the WL and QD GS peak, such that they nearly converge with one another. A comparison of AFM trends to PL spectra can provide a possible explanation for the significant difference in the results of the center PL scan: the thermal profile of the reactor led to a variation in both QD size and optical quality across the $4''$ test wafer. The lower effective growth temperature in the center of the wafer, caused by the susceptor acting as a heat sink, led to a higher density of lower quality smaller dots and shifted the center PL peak towards a higher energy.

Table 2.2: PL peak values and extracted strain and periodicity values from symmetric HRXRD scans. All peak and FWHM values are given in nm.

		Center	Flat-Center	Flat
GaAs	Peak	871	871	872
	FWHM	9	9	10
WL	Peak	932	926	925
	FWHM	97	29	24
QD GS	Peak	975	1004	1004
	FWHM	115	36	33
HRXRD	Strain (ppm)	519	461	407
	Period (nm)	142	141	141

Figure 2.16(a) depicts PL spectra corresponding to pre- and post-ELO scans used to investigate changes in QD emission energies and relative transition strengths following ELO. The GaAs substrate emission maintained a consistent full width at half maximum (FWHM) of $12\,\mathrm{nm}$, and the WL and QD GS transitions maintain a FWHM pre- and post-ELO between $30\,\mathrm{nm}$ and $40\,\mathrm{nm}$, indicating no significant change in size distribution of the QDs during ELO.

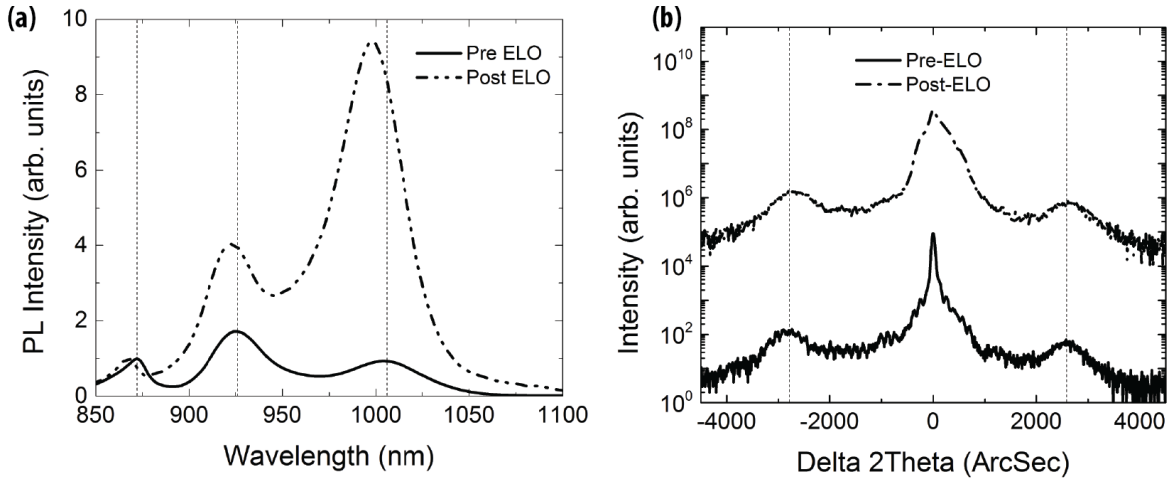

Figure 2.16: PL (a) and HRXRD (b) spectra for a test structure pre- and post-ELO.

Furthermore, the PL results illustrate a strong PL intensity corresponding to the QD ground state energy post-ELO. This could be due to less GaAs material on top of the dots in the post-ELO configuration, which may be increasing the pump power into the QD ground state. However, it is logical to assume that this would also cause the WL peak intensity to increase as well, which would keep the ratio of the two intensities constant. There are two possible interactions that could cause this change: one, the removal of the thick substrate could have an effect on the superlattice strain and the optical coupling between the wetting layer and QDs, which could account for the ratio difference. However, there is still $1\text{-}2\,\mu\mathrm{m}$ acting as a "substrate" following lift-off, which is a significant amount of material when compared to the $\sim 100\,\mathrm{nm}$ intrinsic region containing the superlattice. The more likely possibility is that the QD GS peak observed in the PL is lined up with a cavity mode that is enhanced because of the thin device. The cavity resonance would lead to an effective optical enhancement of light

into the QDs. This enhanced spontaneous emission has been previously observed in QD microcavities and would occur in the current situation if the QD GS peak is near a cavity mode in the thin wafer [48]. In addition, a $4\text{-}5\,\mathrm{nm}$ blue shift in all three peaks was observed. This is likely related to a net change in strain of the GaAs substrate post-ELO and is not due to a change in size of the QDs, which would only affect the position or shape of the QD GS peak. The pre- and post-ELO PL results are compared in Table 2.3.

Table 2.3: ELO comparison of PL peak values and extracted strain and periodicity values from symmetric HRXRD scans. All peak and FWHM values are given in nm.

		Pre-ELO	Post-ELO
GaAs	Peak	871	867
	FWHM	9	12
WL	Peak	926	923
	FWHM	29	34
QD GS	Peak	1004	998
	FWHM	36	33
HRXRD	Strain (ppm)	519	178
	Period (nm)	142	143

Figure 2.16(b) shows HRXRD measurements taken prior to and following ELO. The broadening of the bragg peak post-ELO can be explained by the difficulty of the measurement on a thin foil: the thin structures were delivered on silicon carriers, but rigidity was still an issue. Additional attempts at adhering the foils flat to the chuck proved difficult as well. Periodicity and strain values calculated using the data are also tabulated in Table 2.3. The difference in periodicity between the samples is relatively insignificant, but calculated strain values show that the sample tends to become less

compressive (more tensile) following ELO. This can be due to the lack of a thick substrate, as some relaxation is occurring in agreement with the peak wavelength shift observed in the PL spectra in Figure 2.16(a). A series of additional calculations was performed involving the vertical component of strain (the component measured using this HRXRD technique) and a QD material behaving Poisson's relation that resulted in an approximate strain value necessary to cause a PL peak wavelength shift. Assuming a pure InAs QD in GaAs having a diameter of $20\,\mathrm{nm}$ and height of $3\,\mathrm{nm}$, a tensile strain of approximately $1000\,\mathrm{ppm}$ is needed to cause the 4-$5\,\mathrm{nm}$ blue-shift observed in PL.

Overall, the PL, AFM, and HRXRD analyses indicate that QD optical qualities and material qualities including QD size and superlattice periodicity are maintained post-ELO. These techniques and the conclusions drawn can be aided and expanded by performing a transmission electron microscopy (TEM) analysis of a device structure, which is used to take close-up images of the QD device structure to investigate defects and dislocations that would impact performance. Threading dislocations that arise from misfits and other nonideal morphologies like stacking faults can lower carrier concentrations and mobilities, resulting in device degradation. Ohring notes that the defect level threshold for minority-carrier devices is around $10^3\,\mathrm{cm}^{-2}$, as increasing numbers of defects act as charge-recombination centers, reducing photon radiative processes as well as minority carrier lifetimes and quantum efficiencies [49].

Several cross-sectional TEM images of two QD ELO devices were taken, labeled as sample A and sample B, and used to investigate layer composition and thickness.

Sample A is located spatially near the flat-center of the wafer, and Sample B is located near the center (refer to Figure 2.11). Unfortunately, no baseline devices were measured by TEM for comparison of the inclusion of the superlattice. Furthermore, without performing additional TEM measurements on devices prior to ELO it is difficult to conclude if the dislocations seen are a product of inherent strain fields in the QD devices or are merely a result of intense handling of the thin ELO foils.

Figures 2.17(a) and 2.18(a) each depict a cross-sectional (220) dark-field TEM image of the entire QD ELO device structure, while Figures 2.17(b) and 2.18(b) show a cross-sectional (200) dark-field TEM image of the QD superlattice. In these images, the different layers of the cell as well as the growth direction [100] are annotated. Table 2.4 summarizes the thicknesses of both TEM images, measured using the imaging software ImageJ [50], and compares them to the growth design. The image contrast using this diffraction condition is sensitive to both composition and strain variations. In particular, strain relaxation at the surface of the thin TEM foil gives rise to strong delineation at the interfaces between adjacent, heteroepitaxial layers. Strain-driven tilting and bending of the foil as well as thickness variations also contribute to the contrast.

Dislocations were observed in both Figures 2.17(a) and 2.18(a). Figure 2.17(a) contains threading dislocations that begin along a misfit line at the superlattice interface and then thread along an angle into the base. Figure 2.18(a) appears to have a more significant amount of damage to the base, resulting in a shearing of the lattice structure that manifests as cracking of the foil. The more pronounced damage to

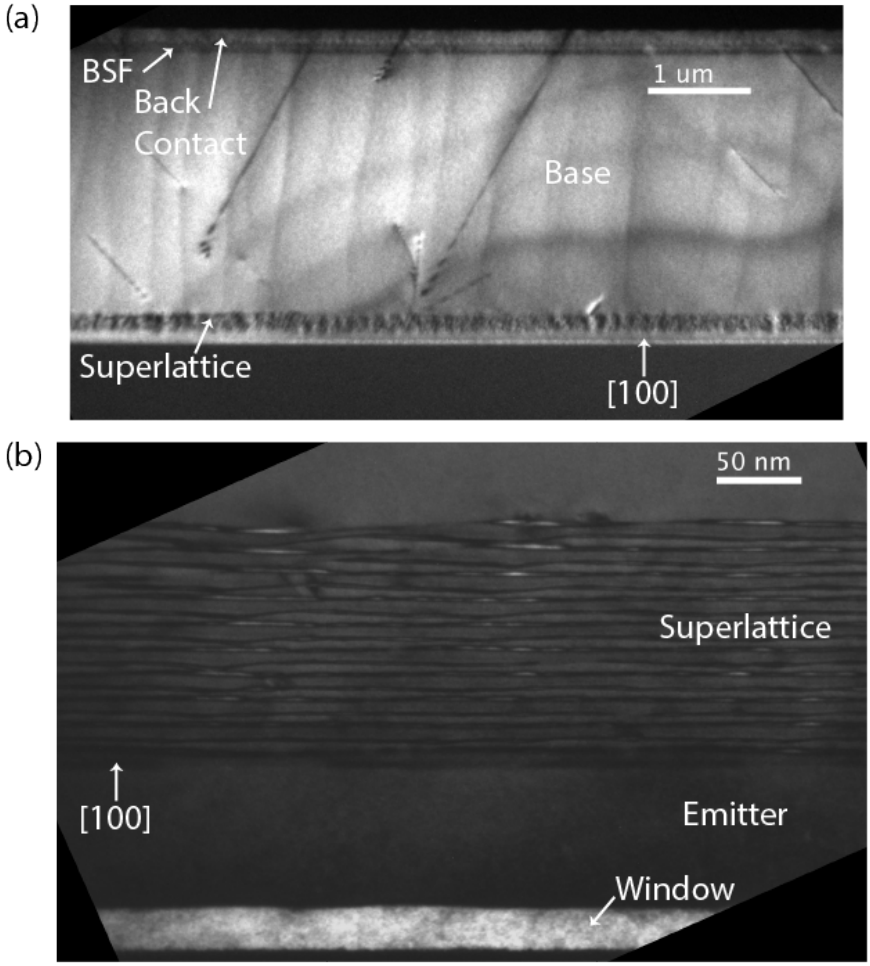

Figure 2.17: Transmission electron microscopy images of (a) the full layer structure and (b) the superlattice for QD ELO sample A.

Table 2.4: Lengths of different layer thickness (all in nm) for two QD devices compiled in ImageJ compared to growth design. The emitter and base regions include the $33\,\mathrm{nm}$ *i*-GaAs region, as this is difficult to measure in TEM alone.

	Window	Emitter	Superlattice	Base	BSF + Back Contact	Total
Growth	30	83	145	2533	260	3051
Sample A	27	83	147	2550	243	3066
Sample B	30	95	148	2700	224	3170

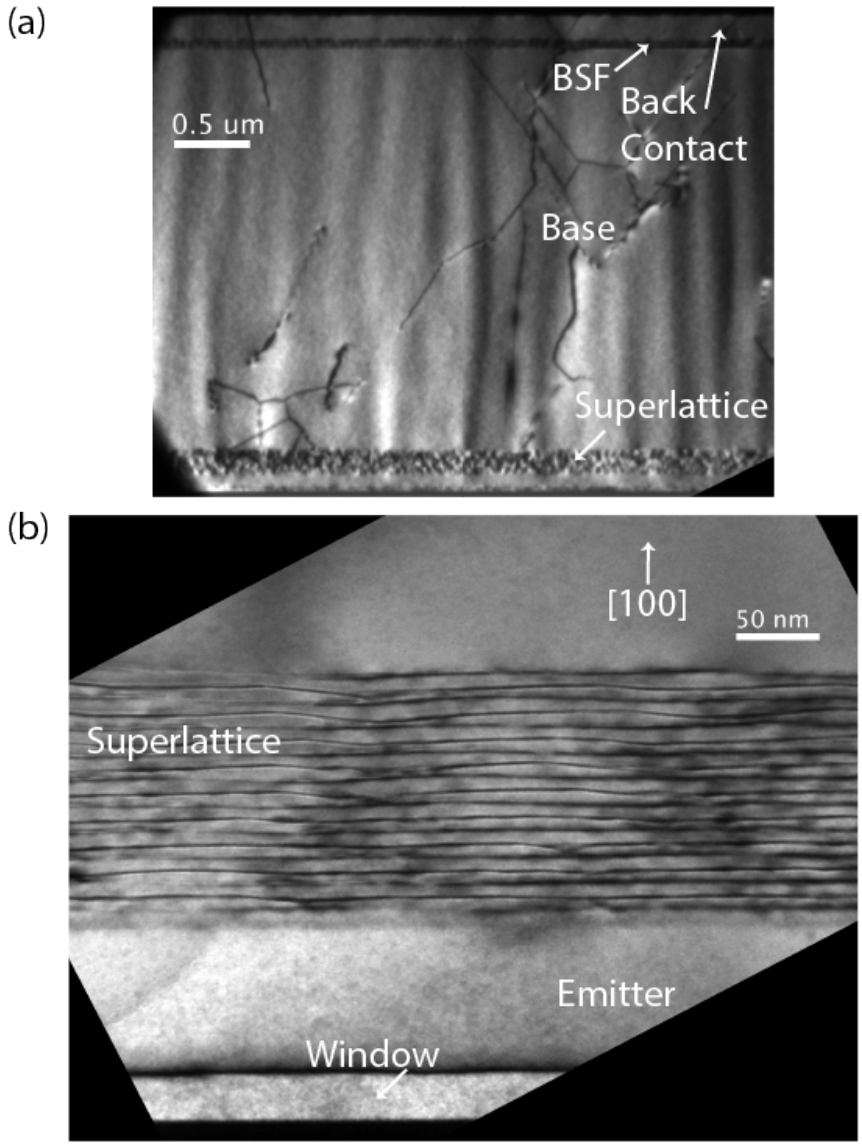

Figure 2.18: Transmission electron microscopy images of (a) the full layer structure and (b) the superlattice for QD ELO sample B.

the base region as observed in TEM seems to lead to a systematic reduction in the quantum efficiency of QD devices grown on $4''$ wafers in a similar location, which will be discussed more in depth after a presentation of device results. Dislocations similar to the V-shaped threads observed in Figure 2.17(a) have been previously observed

in *p-i-n* structures with 5 QD layers with no strain compensation [51] that originate in buried QD layers and travel on different planes to the surface [52].

The superlattices observed in Figures 2.17(b) and 2.18(b) appear to have poor interface quality. In both, the darker areas are defined by the localized strain fields of the InAs QDs. The repeat layers seem to ”bunch up” around some of these areas, which leads to an inconsistent repeat layer thickness perpendicular to the growth direction. This could be caused by stacking faults propagating from the superlattice-emitter interface, or from low-angle grain boundaries caused by quantum dot island coalescense. This could also be a result of an increased temperature profile in this region of the wafer due to the reactor used (as has been previously discussed). A higher apparent growth temperature can lead to larger dots and corrugated interfaces of the superlattice [53].

Figure 2.19 shows a zoomed-in image of the superlattice for sample B. Here, the growth direction is depicted as well as the materials used in the superlattice stack. GaAs spacer layers and GaP strain balancing layers have thicknesses that closely match growth design parameters. Measured parameters are compared to growth design in Table 2.4. The total superlattice thickness of 150 nm is also consistent with periodicity values calculated using high resolution X-ray diffraction measurements, as explained previously.

The TEM in Figure 2.19 shows QD stacking that appears to occur on a 25° degree angle to the (100) plane. As discussed by Shoji et al. [54], this QD alignment is tilted along a direction of a stronger non-local center of strain, as is visible in the TEM.

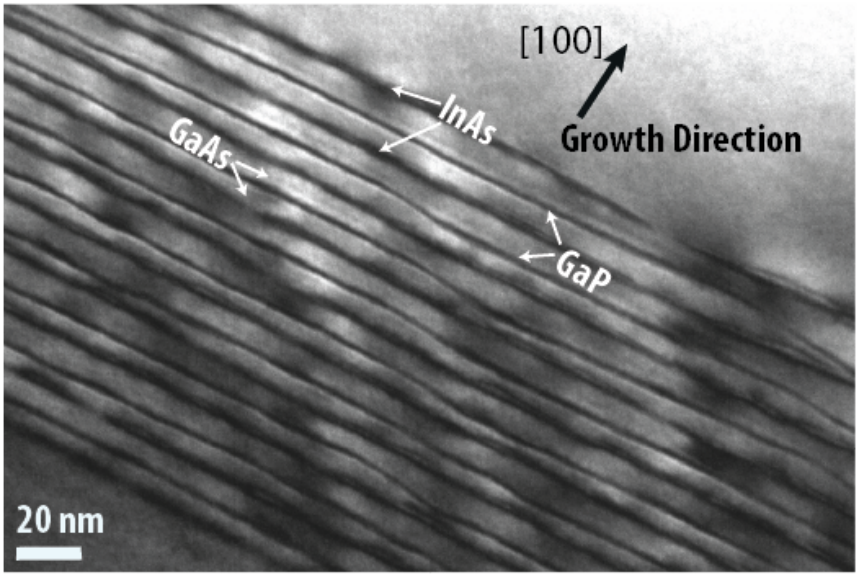

Figure 2.19: Transmission electron microscopy images of the zoomed in QD superlattice of sample B. Materials used in the superlattice layer stack are labeled.

The strain arises from the buried dots, although the strain compensation layers aid in mitigating induced strain at each layer surface. When present in lower layers, this strain tends to affect the QD formation in higher layers and could have a significant effect on the overall optical absorption properties of the QD ensemble.

2.3.2 Statistical Current-Voltage Characteristics and Discussion

As explained previously, current-voltage metrics are a valuable indicator of solar cell device performance. Many cells on both the baseline and QD ELO cells were measured to obtain a statistical spread in solar cell figures of merit. Overall, 55 0.5x0.5 cm^2 devices were measured on the baseline wafer and 37 devices were measured on the QD wafer, shown in Figure 2.20.

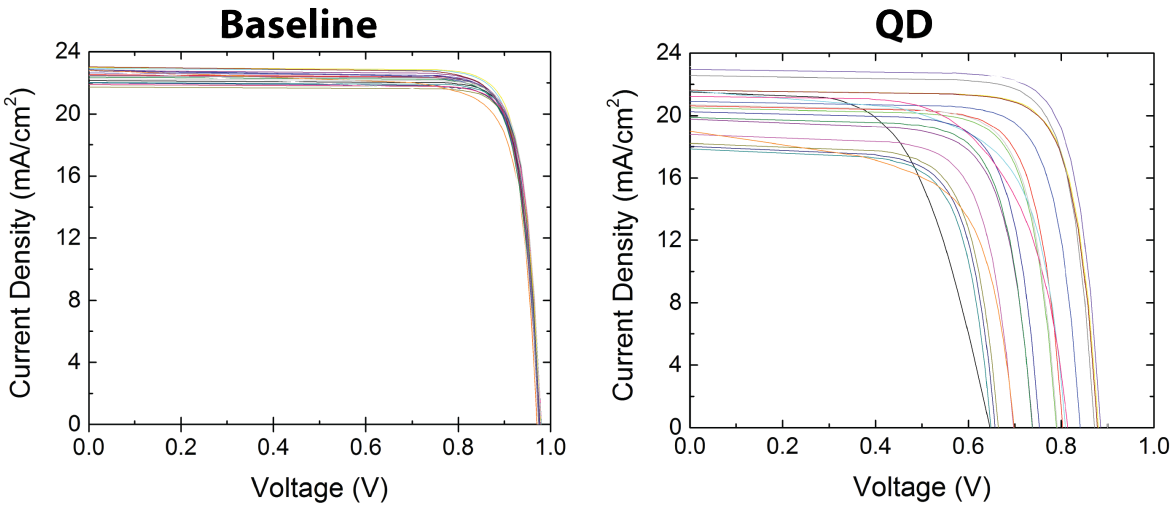

Figure 2.20: Multiple J-V curves for both baseline and QD ELO devices depicting wafer uniformity. The QD wafer has a significantly higher degree of non-uniformity in both J_{sc} and V_{oc}.

The QD measurements show a much larger spread in solar cell J-V metrics, while baseline samples maintain a more consistent profile although there is some spread in J_{sc} as well. Box plots were created to display the statistical spread of the baseline and QD devices for J_{sc}, V_{oc}, FF, and η, shown in Figure 2.21. In each of these plots, the box signifies the 25^{th}-75^{th} percentile, and the whiskers expand out to the 5^{th} and 95^{th} percentiles. The line inside each box describes the median, while the square inside the box is the mean. The crosses at either extreme are the minimum and maximum values for the sample set. Statistical spreads for solar cell metrics across the two wafers are summarized in Table 2.5.

For a comparison of wafer uniformity, Figure 2.22 shows baseline and QD ELO J_{sc} and V_{oc} performance for devices measured around the $4''$. The baseline ELO devices all exhibit a small spread across the wafer, and there does not seem to be an overall spatial dependence. J_{sc} values are slightly higher towards the middle of the wafer and

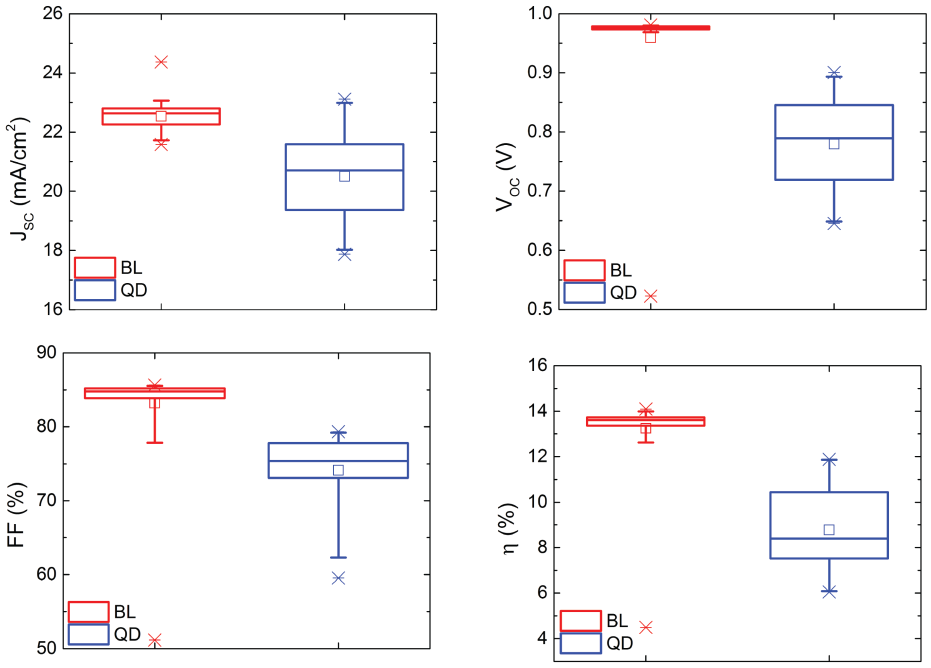

Figure 2.21: Box plots showing statistical uniformity for baseline and QD wafers for solar cell figures of merit: J_{sc} (top left), V_{oc} (top right), FF (bottom left), and η (bottom right).

Table 2.5: IV 1-Sun AM0 Statistical Results

		J_{sc} ($\mathrm{mA/cm^2}$)	V_{oc} (V)	FF (%)	P_{max} ($\mathrm{mW/cm^2}$)	η (%)
Baseline	Average	22.5	0.96	83.2	18.1	13.3
	Std Dev	0.5	0.08	5.8	2.3	1.7
QD	Average	20.5	0.78	74.1	12.0	8.8
	Std Dev	1.5	0.08	5.0	2.5	1.8

trend downward toward the outer edge. V_{oc} across the wafer is also consistent, and almost all devices exhibited open circuit voltage values greater than $0.97\,\mathrm{V}$. The QD ELO wafer exhibits a much different performance across the wafer. Both J_{sc} and V_{oc} are much lower in the middle of the wafer, and trend to higher values radially outward from the center. The best performing QD ELO cells were therefore closest to the wafer edge. Recall in the previous section and Figure 2.15 that the center PL scan

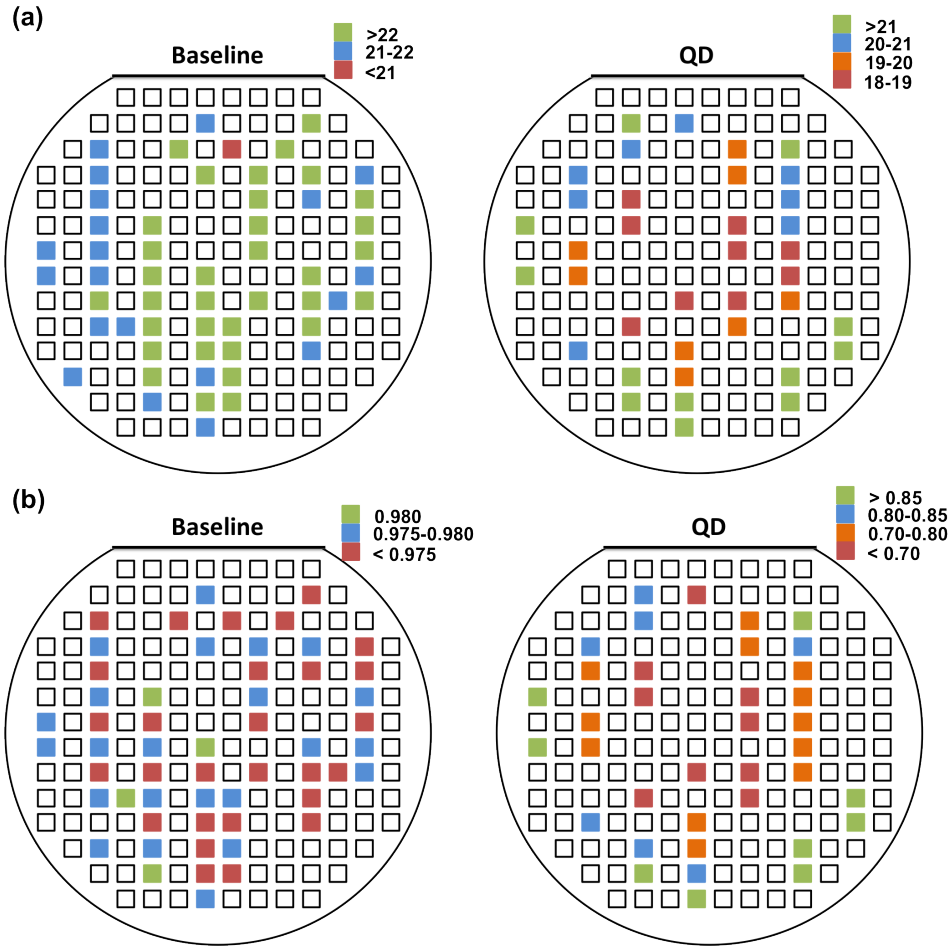

Figure 2.22: Variation of solar cell metrics (a) J_{sc} (mA/cm^2) and (b) V_{oc} (V) of devices measured around the wafer.

and AFM micrograph exhibited different results than those toward the outer edge of the wafer, near the flat. It was hypothesized that this was due to the reactor used during growth, in which the thermal profile of the platen and susceptor used to hold the wafer translated to a lower local temperature for QD growth in the center of the wafer. This led to a larger density of dots with smaller heights that were of lower quality in the center of the wafer. Clearly, the temperature profile of the reactor has also led to poor device performance of QD ELO cells in the center of the wafer.

Figure 2.23 depicts dark J-V curves of two baseline ELO and two QD ELO solar cells. Extracted values for reverse saturation current J_0, ideality factor n, and parasitic resistances are summarized in Table 2.6. Ideality factors are near 2, indicating that recombination mechanisms are limited by two-carrier processes. It is apparent that the QD ELO cells have a higher and more varied dark current than baseline ELO solar cells. This ultimately leads to a variation in V_{oc}, which was observed in light J-V measurements. Referring back to Figure 2.22, QD 1 is near the top left of the wafer, while QD 2 is near the anti-flat center (recall Figure 2.11) location of the wafer. QD 2 exhibits poor light J-V characteristics as well as dark J-V, highlighted by the greater effect of parasitic resistances and a J_0 value that is nearly an order of magnitude larger than QD1. Even so, QD1 underperforms when compared to dark J-V results of the two baseline cells, which exhibit a lower R_s, higher R_{sh}, and J_0 values that are an order of magnitude lower than QD1.

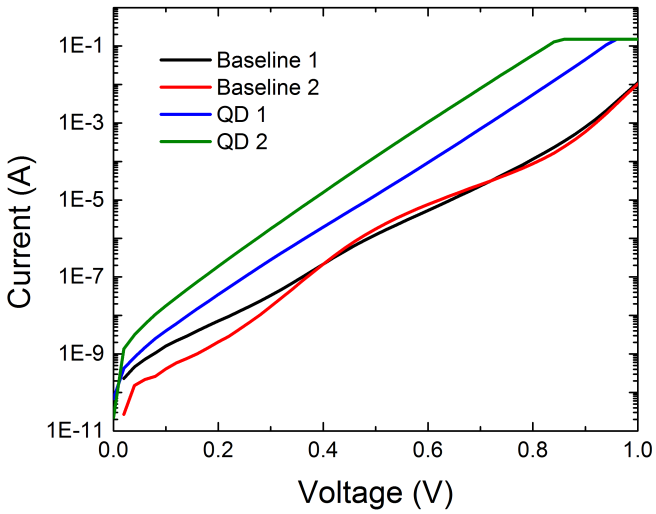

Figure 2.23: Dark J-V curves measured during a J_{sc}-V_{oc} test and used to extract reverse saturation current densities and ideality factors for ELO devices.

Table 2.6: Dark J-V results. A small increase in R_s and similar decrease in R_{sh} can change J_0 by almost an order of magnitude, as noted in the QD results.

Sample	J_0 (pA)	n	R_s (Ω)	R_{sh} ($\mathrm{M}\Omega$))
Baseline 1	24.3	2.02	0.88	83.2
Baseline 2	18.5	2.02	0.87	132.0
QD 1	768	1.97	1.32	30.0
QD 2	3450	1.82	2.04	18.8

2.3.3 Statistical Spectral Responsivity Measurements and Electrical Observations

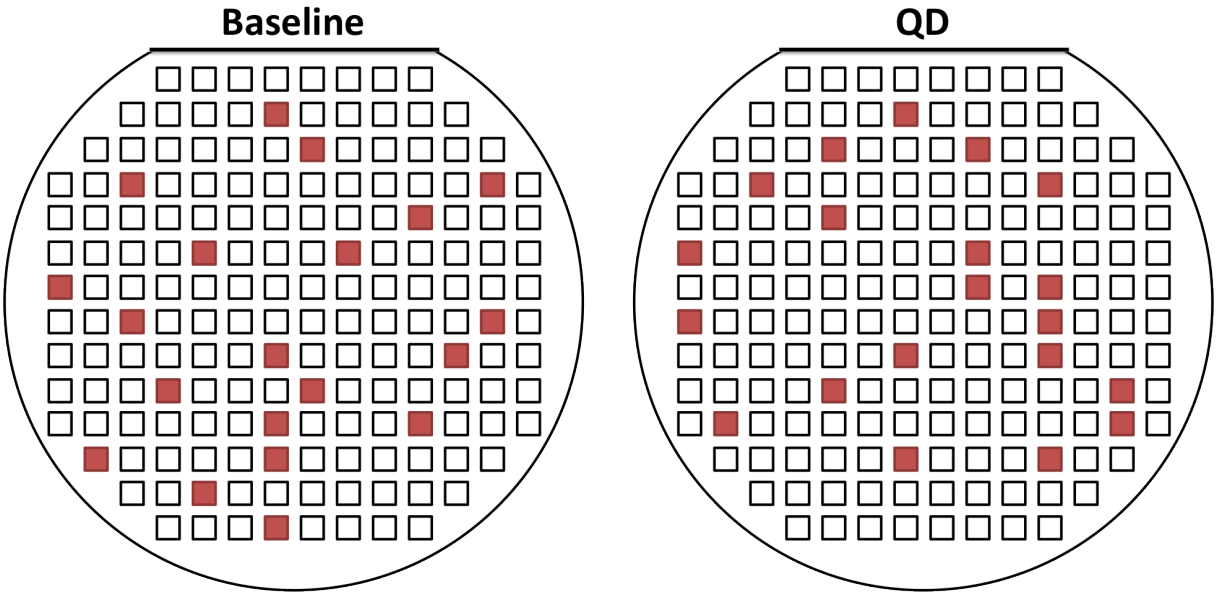

Figure 2.24: Positions of cells measured around the wafer.

Following the J-V measurements, 20 cells were chosen to calculate statistical distributions in spectral responsivity measurements across each wafer. The locations of the cells that underwent SR testing are shown in Figure 2.24. External quantum efficiency (EQE), calculated from spectral response, can more effectively convey the absorption and collection yield across incident wavelengths and aid in quantifying the QD contribution to the short circuit current density. EQE plots for baseline and QD ELO

devices are shown in Figure 2.25. The EQE plots clarify the varying degree of J-V performance by many of the QD ELO cells, as will be discussed. Short circuit current densities were calculated from spectral response using Equation 2.11 as explained in the previous section using a trapezoidal numerical integration, and are shown and compared with J_{sc} values from J-V measurements under the solar simulator in Figure 2.26.

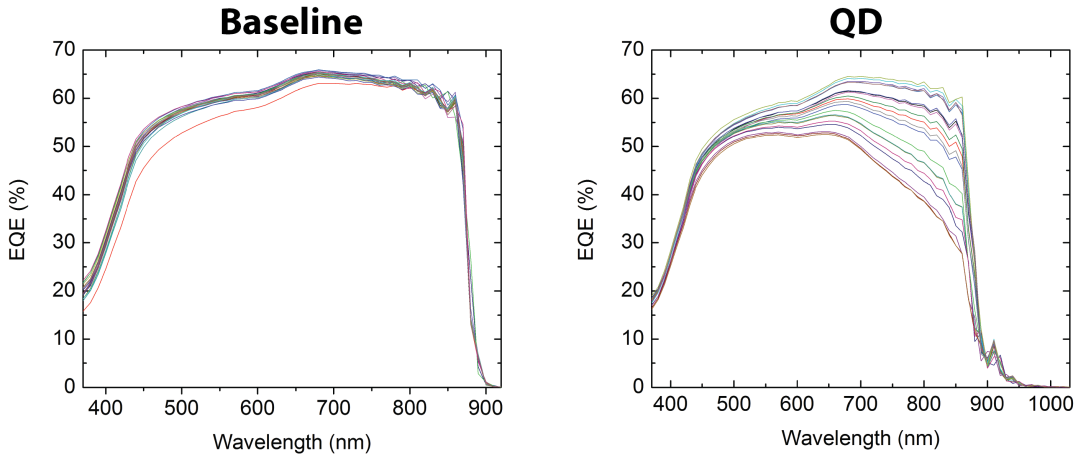

Figure 2.25: EQE curves showing variations in carrier absorption and collection for baseline and QD ELO devices. The QD wafer non-uniformity seen in AM0 J-V results is largely related to a significant degradation in base collection in several cells.

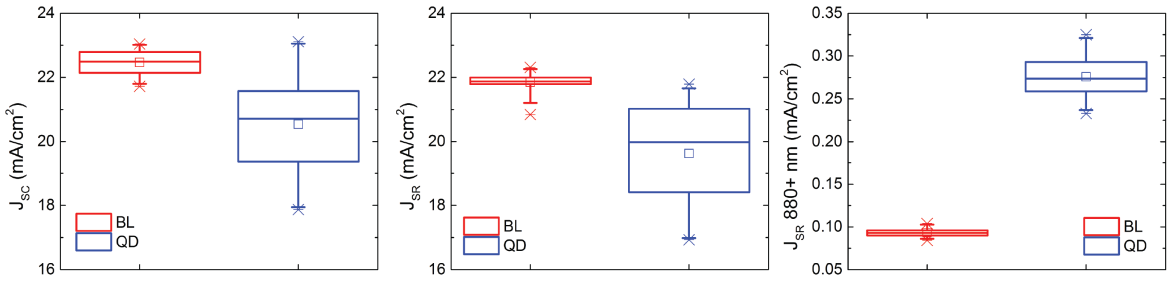

Figure 2.26: Box plots comparing J_{sc} values obtained from AM0 LIV measurements (left) with those calculated through integrated spectral response (J_{SR}) for the entire device (middle) and only the QD contribution for $880+\,\mathrm{nm}$ (right).

Table 2.7: J-V Performance Metrics Of 20-Device Sample Set Used For Statistical EQE Measurements.

		J_{sc} ($\mathrm{mA/cm^2}$)	V_{oc} (V)	FF (%)	P_{max} ($\mathrm{mW/cm^2}$)	η (%)	J_{SR} [bulk] ($\mathrm{mA/cm^2}$)	J_{SR} [$\lambda > 880\,\mathrm{nm}$] ($\mathrm{mA/cm^2}$)
Baseline	Average	22.5	0.976	84.1	18.4	13.5	21.9	0.093
	Std Dev	0.4	0.003	2.0	0.4	0.3	0.3	0.005
QD	Average	20.5	0.775	73.3	11.8	8.7	19.6	0.276
	Std Dev	1.6	0.086	5.7	2.7	2.0	1.6	0.026

It is useful to visualize not just how an incoming photon at a given energy will generate an electron-hole pair, but at what depth in a device. Shorter wavelength, or high energy photons, will be absorbed at a smaller depth than long wavelength, or low energy photons. Therefore, EQE spectra are typically split up into the regions of the device, thus as a simplistic example shorter wavelengths (400-700 nm) correspond to emitter absorption, and longer (700 nm - near the bandedge) correspond to base absorption. Increased absorption past the GaAs bandedge observed in the QD ELO cells is due to the QD superlattice. In many QD cells significant base degradation was observed, leading to the varying integrated J_{sc} values. This could be due to residual strain in the superlattice prior to ELO, which affected the minority carrier diffusion length and other optical properties of the base.

Table 2.7 summarizes the statistical averages and 1-sigma standard deviation values of the smaller set of baseline and QD ELO devices used for spectral response measurements. It is clear that a severe reduction in EQE has lead to a degradation in J_{sc} and V_{oc} for several QD ELO cells across the wafer. Measured EQE both in the bulk as well as beyond the GaAs bandedge ($\lambda >$880 nm) was convolved with the AM0 solar spectrum in space (ASTM E-490) in order to quantify the QD contribution to J_{sc}. The

calculation follows Equation 2.11, and these values are also included in Table 2.7. In order to pinpoint a more definite reason for the overall QE reduction for the QD ELO devices as compared to the baseline ELO devices, a MATLAB program was used to model the EQE plots.

A drift-diffusion MATLAB model was used to investigate the variation in cell performance across the wafer. Equations following the Hovel-Woodal model outlined previously were used to extract diffusion length values for all experimental EQE curves. Due to testing difficulty in making sure the exact same spot in each cell was being measured, as well as a variation in grid shadowing across many cells, the EQE measurements have an inherent statistical variation. Overall, reflectance may vary from shape to shape and magnitude may be different depending on the sample. Since not all samples had corresponding reflectance measurements, a single reflectance file was used for all simulations. For all simulations, surface and interface recombination velocities were held constant, and only lifetime values were varied to fit the simulated curve shape to the experimental data. Figure 2.27 shows example simulation curves obtained using the model for both a baseline and QD ELO device.

The model is able to show the specific contribution to the total curve that is obtained in the window, emitter, space-charge, and base regions of the device. Also included on each curve are the reflectance used in the simulation as well as the experimental data. Both simulations gave a good match to the experimental data. Figure 2.29 as well as Table 2.8 help to quantify the degree of variation of EQE measurements shown in Figure 2.25. The experimental EQE curves from the sample set were modeled to

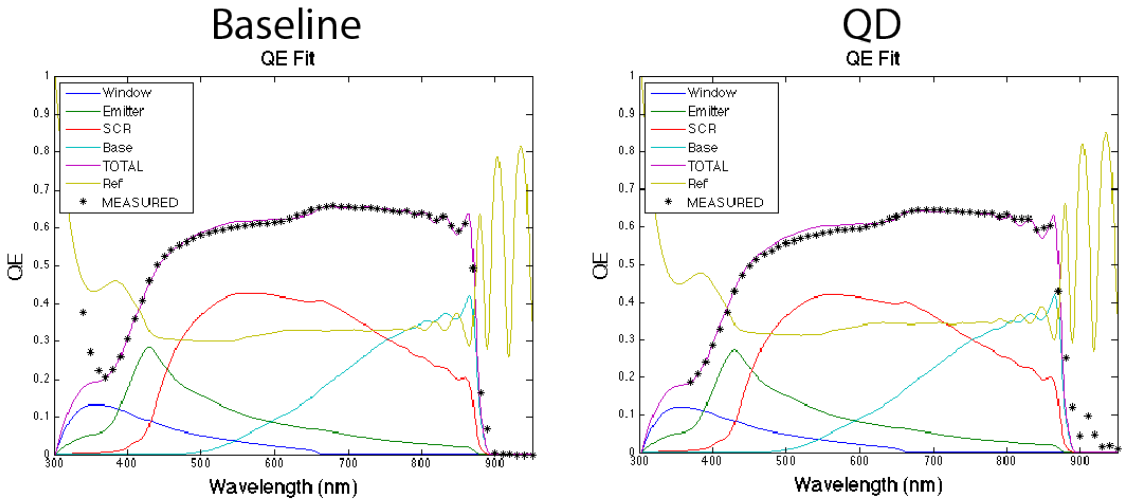

Figure 2.27: MATLAB simulations following the Hovel-Woodal model to fit experimental EQE data and extract out carrier transport properties.

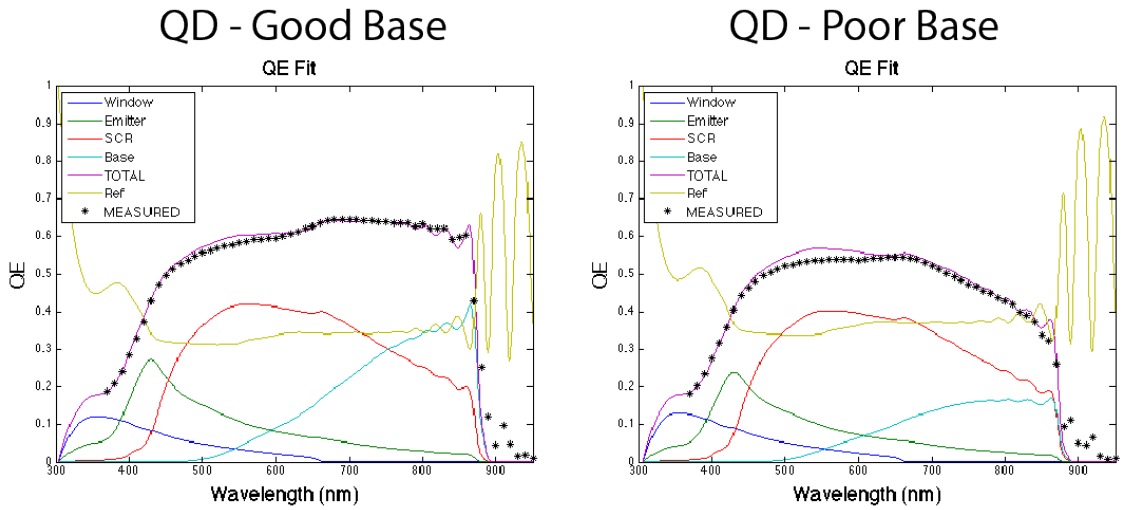

Figure 2.28: MATLAB simulations following the Hovel-Woodal model to fit experimental EQE data and extract out carrier transport properties.

extract diffusion lengths in the emitter and base regions of each device. Clearly, there is a large variation in the diffusion length in the base region of the QD curves. Figure 2.28 shows two simulations of QD devices with significantly different base responses side by side. Similar to the two QD ELO cells described in the dark J-V discussion

(Figure 2.23), the ”good base” QD cell is located near the top left of the wafer, while the ”poor base” QD cell is near the anti-flat center location of the wafer. The ”good base” QD device operates with a minority carrier diffusion length in the base of over $6000\,\mathrm{nm}$ compared to the ”poor base” QD cell value of less than $1000\,\mathrm{nm}$. The ”good base” device is on the order of the baseline devices modeled, showing that the best performing QD ELO devices are comparable to the baseline devices. High efficiency devices from the QD ELO and baseline ELO devices are compared in the following section.

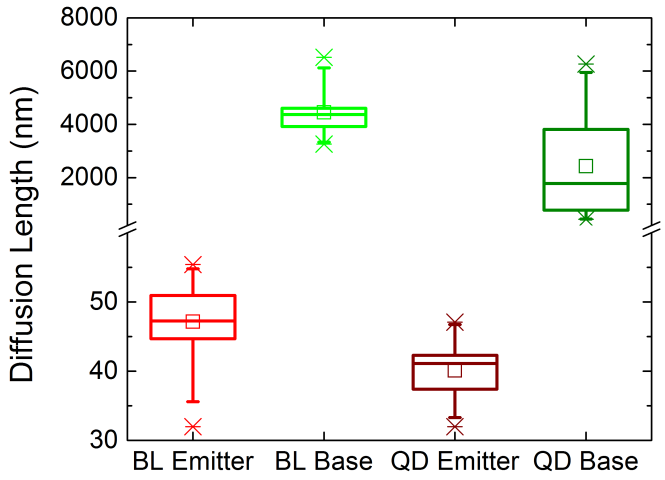

Figure 2.29: Box plots of modeled emitter and base minority carrier diffusion lengths for the sample set of EQE measurements performed. Baseline ELO cells outperform QD ELO cells on average due to longer diffusion lengths that allow for improved carrier transport.

Table 2.8: Diffusion Lengths Simulated using MATLAB Drift-Diffusion Model

		Emitter (nm)	Base (nm)
Baseline	Average	50	4450
	Std Dev	5	790
QD	Average	40	2430
	Std Dev	4	1930

2.3.4 Comparison of Best Performing Cells Across The $4''$ ELO Wafers

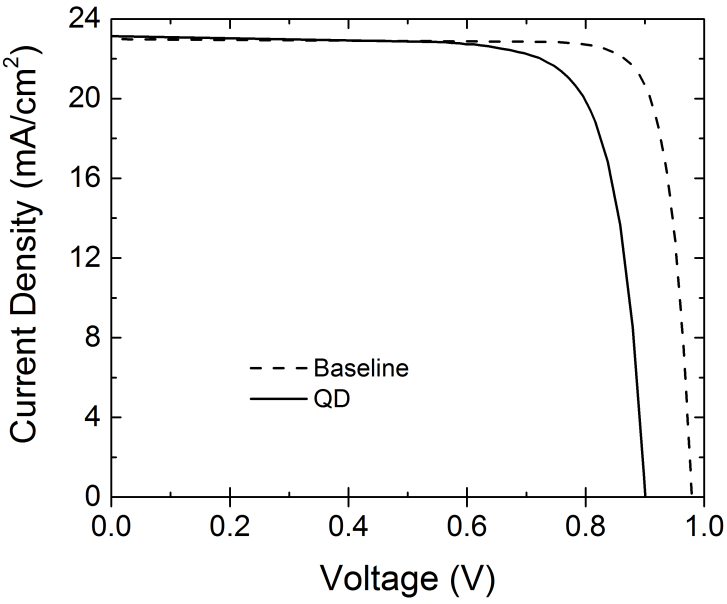

Figure 2.30: High-efficiency device chosen from baseline and QD sample for comparison. A current enhancement is seen in the QD device as well as a decrease in V_{oc}.

Figure 2.30 shows the J-V curve of best-performing cells across the $4''$ baseline and QD ELO wafers for comparison. The solar cell metrics for these solar cells are shown in Table 2.9. Comparison of these values indicates an absolute $0.12\,\mathrm{mA/cm^2}$ increase in short circuit current density (J_{sc}) for the QD device when compared to a similar baseline device and an $80\,\mathrm{mV}$ decrease in open circuit voltage (V_{oc}). The loss in V_{oc} can be attributed to residual strain from the QD superlattice on the overall structure as well as increased non-radiative recombination that comes from the inclusion of the QDs. Additionally, adding QDs decreases the effective bandgap of the solar cell device, which will result in a lower V_{oc}. Indeed, the fact that the open circuit voltage of the QD ELO cell was maintained at $0.9\,\mathrm{V}$ is a significant improvement over prior

reports [31]. Moreover, the $80\,\mathrm{mV}$ loss in V_{oc} from the baseline ELO device to the QD ELO device is comparable to reported upright *p-i-n* QDSCs, which showed a loss of $60\,\mathrm{mV}$ between the QD and baseline solar cells [55].

Table 2.9: J-V 1-Sun AM0 High Efficiency Device Results

	J_{sc} $(\mathrm{mA/cm^2})$	V_{oc} (V)	FF $(\%)$	η $(\%)$	J_{SR} Bulk $(\mathrm{mA/cm^2})$	J_{SR}, $\lambda > 880\,\mathrm{nm}$ $(\mathrm{mA/cm^2})$
Baseline	23.0	0.98	85	14.0	22.2	0.10
QD	23.1	0.90	78	11.9	21.8	0.33

Altogether, a V_{oc} near $0.9\,\mathrm{V}$ is a very promising initial result for these solar cells, and the modest increase observed in J_{sc} is also promising for a device with only 10 QD layers. Note that while a high-reflectance backside mirror was not implemented in these devices, the bare GaAs to Au rear interface is expected to be nearly 78$\%$ reflective in the near infrared (based on calculation). Index matching of this interface could improve the reflectance to nearly 98$\%$, resulting in further improvement in J_{sc} for the QD ELO device. The reduction in V_{oc} and a lower fill factor for the QD ELO device gives an absolute reduction in efficiency of 2.1% for the QD cell when compared to the baseline. Although promising, J-V results indicate that there is much room for improvement. For instance, strain balancing for these samples was calculated based on results from previous work with traditional, upright QDSCs. Further optimization may be necessary for QD ELO devices, and could lead to an improvement in material quality and V_{oc}.

EQE spectra for the same high efficiency QD and baseline ELO devices compared in Figure 2.30 are shown in Figure 2.31(a). When compared to the baseline device,

the QD cell shows a small collection probability loss at shorter wavelengths (400-700 nm), corresponding to emitter absorption, and a close match near the bandedge corresponding to base absorption. Integrated spectral response values are also shown in Table 2.9. Most importantly, the QD ELO sample shows a significantly increased response for sub-GaAs bandgap wavelengths when compared to the reference cell, indicating that some of the J_{sc} contribution is coming from absorption into QD states. Measured EQE beyond the GaAs bandedge ($\lambda >$880 nm) was convolved with the AM0 solar spectrum in space (ASTM E-490) in order to quantify the QD contribution to J_{sc}, following Equation 2.11. This was calculated to be $0.23\,\mathrm{mA/cm^2}$ after subtracting the residual current density in the baseline cell due to the thermal distribution of carriers at the GaAs bandedge. This contribution is greater than comparable upright devices [45], and can be further enhanced by adding more QD layers or using a high reflectance backside mirror to increase the OPL of the cavity. Additionally, the subband portion of the measured EQE data is expanded in Figure 2.31(b). The plot here shows ELO baseline and QD cells, an upright QDSC (the details of which are described in Chapter 4) for comparison, and an EL spectrum of a QD ELO device. The EL peaks, corresponding to excited states of the QDs, match up in terms of wavelength with the subband response seen in EQE measurements, indicating that the EQE peaks are being amplified by QD cavity modes, and will be discussed further.

The slight EQE loss for the QD samples at shorter wavelengths is due to an incomplete contact layer etch of the QD ELO wafer. As the devices were grown inverted,

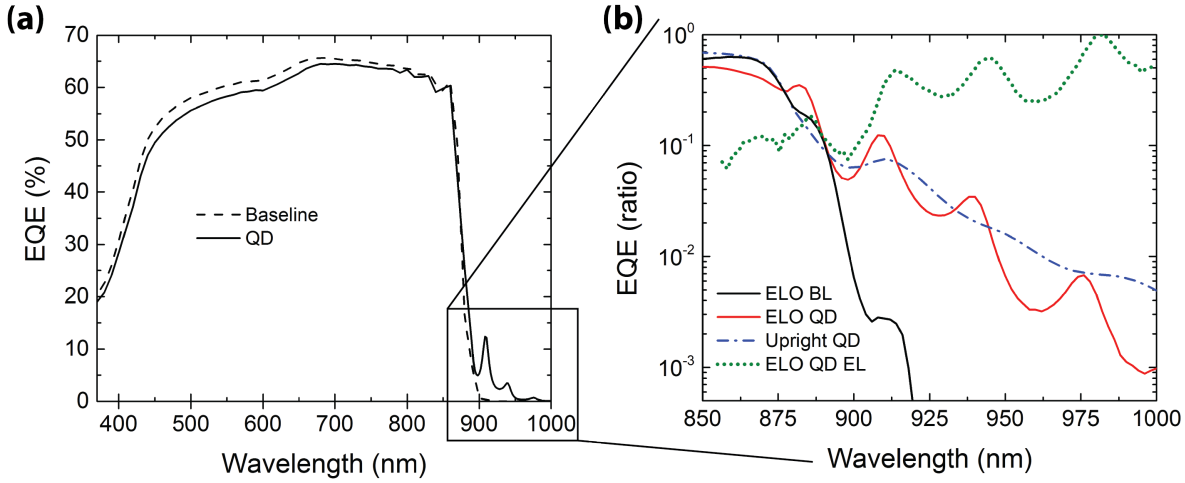

Figure 2.31: External quantum efficiency calculated from spectral response measurements of baseline and QD ELO devices. (a) depicts bulk measurements while (b) zooms in on the sub-GaAs bandedge region of the spectrum, and includes an electroluminescence measurement.

any degradation created by the QD superlattice would logically create threading dislocations that would lead to a decreased response in the base region of the solar cell and thus loss in the QE spectra near the bandedge. An incomplete contact etch would also lead to a smaller J_{sc} value than expected observed in light J-V. Figure 2.32 compares Nomarski images taken of baseline ELO and QD ELO solar cells.

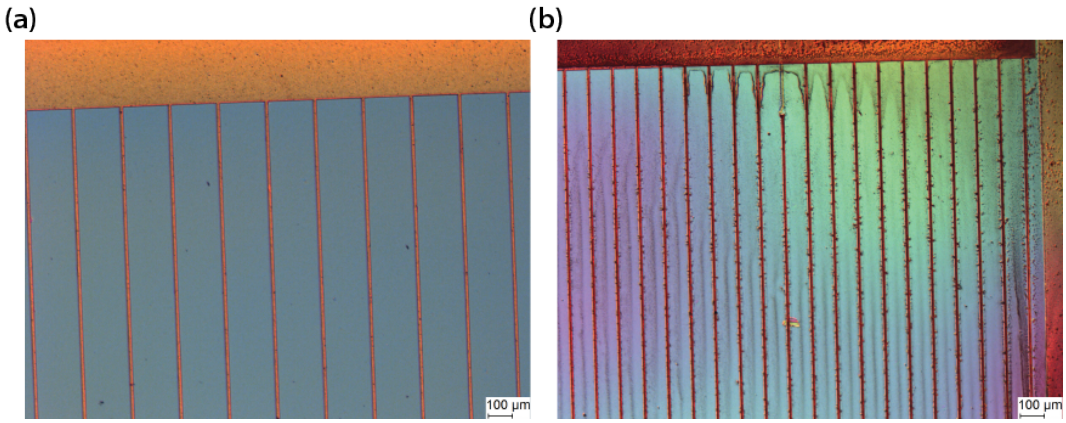

Figure 2.32: Nomarski images comparing similar cell regions from baseline ELO and QD ELO devices. It is clear that the QD ELO wafer suffers from an incomplete contact etch, leading to some current loss in the short-to-mid wavelength region.

It is apparent that there is some residual highly-doped GaAs on the surface of the QD ELO wafer resulting from an incomplete contact etch. This would lead to degradation in current absorption in short-to-mid wavelengths, and could also be one cause of the larger statistical spread in response of the QD ELO devices measured. However, the main cause for the drastic variation in base response and QD device performance is the temperature profile of the reactor.

It is apparent from Figure 2.31 that the QD contribution to the spectral response shows resonant peaks that are strongly enhanced when compared to the traditional upright QD cell [45]. That is, the EQE of sub-GaAs bandedge wavelengths consists of multiple resonant peaks for the ELO cell that are not seen in a *p-i-n* upright QD device. This wavelength region is again zoomed in and depicted in Figure 2.33. This effect is a result of resonant cavity modes that arise due to the thinning of the device. As initially proposed, the ELO process creates an avenue for exploiting light management techniques to enhance the absorption at specific wavelengths. To further demonstrate this, a finite-differential time-domain (FDTD) simulation was performed. The simulated structure was identical to the baseline ELO growth design but with a thick i-region, and included a 2.8 μm bulk GaAs layer with an InGaP front window layer and back surface field, a thin GaAs back contact and a thick Au reflector.

The electric field intensity was simulated at a depth of 150 nm into this structure, where the QDs would be placed, and observed as a function of wavelength to compare to sub bandgap EQE peaks. This simulation is also shown on the plot in Figure 2.33. The well-defined sub-GaAs bandgap peaks in the inset of Figure 2.33 occur

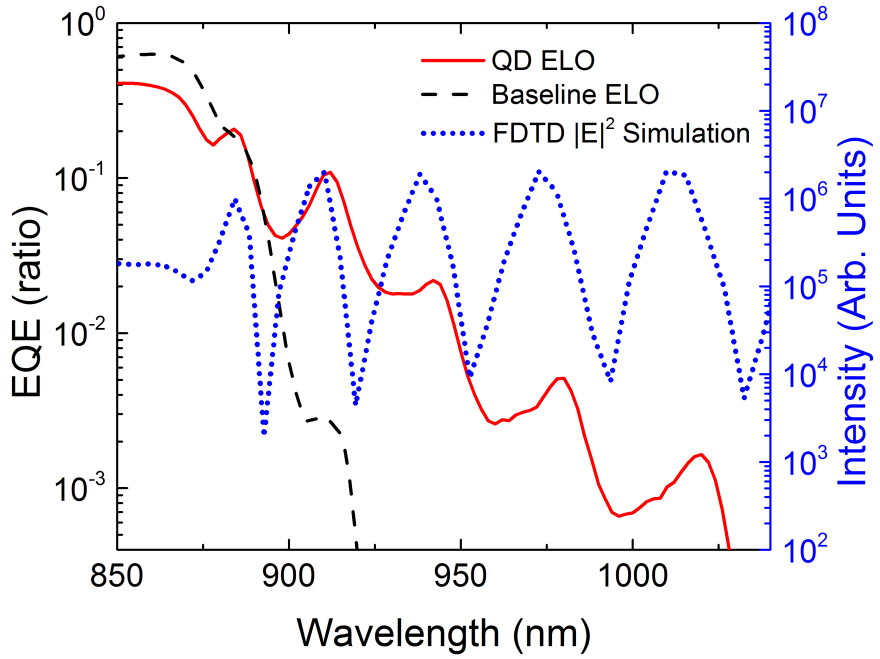

Figure 2.33: Sub-GaAs bandgap EQE curves showing enhanced absorption in the QD states. The blue dotted FDTD simulation is a representation of the electric field intensity in a thin cavity of a similar structure to the ELO devices.

at wavelengths of 882, 908, 939, and 975 nm. The spacing between these peaks increases by 38% at wavelengths closer to the QD GS transition when compared to wavelengths near the GaAs bandedge, and is an observed effect in a Fabry-Perot cavity. Simulated peaks are observed at 884, 906, 938, and 973 nm in close match to experimental values. This indicates that enhancement of the electric field in the infrared (due to the cavity formed by the thin ELO device) can be effectively used to improve QD absorption.

2.3.5 Temperature Dependent Performance

The two main mechanisms for carrier escape from QDs are thermal activation and tunneling [56]. At room temperature, the thermal escape rate is much faster than optical emission from QD states, and is dominant. At much lower temperatures, tunneling becomes a dominant carrier escape mechanism. For solar cells that may be advantageous in space, a study of J-V performance at varying temperatures is useful. Temperature coefficients for both baseline and QD ELO samples were extracted using linear fits for AM0 1-sun J-V curves taken as a function of temperature between 20 and 80 $^{\circ}\mathrm{C}$. The fits were used to extrapolate temperature curves out to $150\,^{\circ}\mathrm{C}$. Both the measured data points and fits are depicted in Figure 2.34, and the extracted temperature coefficients are summarized in Table 2.10.

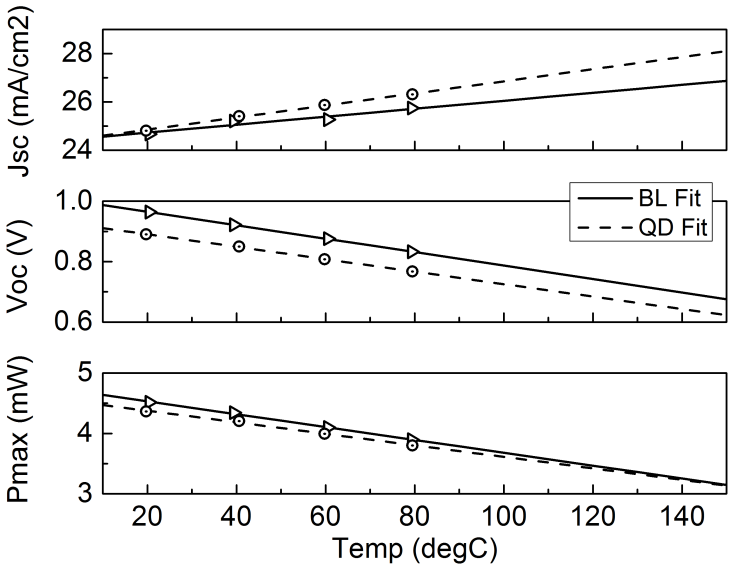

Figure 2.34: Temperature coefficients for J_{sc}, V_{oc}, and P_{max} for baseline and QD ELO samples.

J-V results showed a higher J_{sc} temperature coefficient in the QD cell when compared to the baseline, which has been previously observed in upright QDSCs [57]. As temperature increases, this rate of thermal escape or activation continues to increase, which leads to an increased J_{sc} temperature coefficient for the QD sample. In addition, a slightly higher V_{oc} temperature coefficient was observed in the QD cell when compared to the baseline. An increase in temperature will cause the bandgap of a semiconductor to decrease. The fact that the V_{oc} decreases less as temperature increases may indicate that QDs are less affected by bandgap temperature dependence. Overall, this gave a $\mathrm{P_{max}}$ temperature coefficient increase of $1\,\mu\mathrm{W/^{\circ}C}$ for the QD sample as compared to the baseline, which is a relative increase of $10\,\%$.

Table 2.10: Summary of IV temperature coefficients for ELO cells under 1-sun AM0 conditions, percentage difference for the QD sample relative to the baseline sample is shown for comparison.

	J_{sc} (μA/°C)	V_{oc} (mV/°C)	P_{max} (μW/°C)	FF (%/°C)
Baseline	4.12	-2.23	-10.64	-0.052
QD	6.25	-2.06	-9.53	-0.064
Rel. %	51.8	7.5	10.4	-21.9

2.4 CONCLUSIONS

In summary, InAs/GaAs QD-ELO solar cells were grown and fabricated to yield thin solar cells with an increased collection and absorption in sub-GaAs bandgap wavelengths. The devices included 10 layers of QDs in the i-region of the cell, forming a

QD superlattice in the bulk GaAs matrix. This degree of stacking can be extended to increase the filling factor of the QD superlattice. In order to investigate how the ELO process affects both optical and material qualities, test structures were grown that included 5 layers of QDs. The test structures were characterized by AFM, PL, and HRXRD and then processed via ELO. The thin foil structures were characterized post-ELO using PL and HRXRD. Optical and materials characterization and analysis of test structures showed a successful ELO transfer with QD structures, but also that growth conditions will need to be further optimized to obtain a sufficient degree of uniformity across a $4''$ wafer.

Analysis of device characterization using J-V characterization gave ranges of several solar cell metrics across the wafer. The J_{sc} of baseline ELO samples ranged from $22.4 \pm 0.4\,\mathrm{mA/cm^2}$, and for the QD samples $20.5 \pm 1.6\,\mathrm{mA/cm^2}$. The V_{oc} measured were $0.976 \pm 0.003\,\mathrm{V}$ for the baseline ELO samples and $0.775 \pm 0.086\,\mathrm{V}$ for the QD ELO samples. The calculated efficiencies under 1-sun conditions for the 0.5x$0.5\,\mathrm{cm^2}$ cells were $13.5 \pm 0.3\,\%$ for the baseline ELO devices measured and $8.7 \pm 2.0\,\%$ for the QD ELO devices. The best QD ELO cell had a higher short circuit current density when compared to the baseline cell by an absolute value of $0.12\,\mathrm{mA/cm^2}$.

EQE statistical measurements yielded an integrated short circuit current value for baseline devices of $21.9 \pm 0.3\,\mathrm{mA/cm^2}$, and $19.6 \pm 1.6\,\mathrm{mA/cm^2}$ for the range of QD devices measured. Only wavelengths greater than $880\,\mathrm{nm}$ were also convolved with the AM0 spectrum to quantify the QD contribution to the short circuit current density. For baseline ELO devices, there is a thermal tail of carriers at the bandedge, so the value

is nonzero. This integrated value is $0.093 \pm 0.005\,\mathrm{mA/cm^2}$. QD samples had a significantly higher subband absorption spectrum, and integrated to $0.276 \pm 0.026\,\mathrm{mA/cm^2}$. The integrated EQE past the GaAs bandedge for the QD ELO cell after subtracting out the baseline ELO value for the best cells measured was $0.23\,\mathrm{mA/cm^2}$ due to QD photocurrent enhancement.

Chapter 3

Radiation Effects in ELO QDSCs

3.1 MOTIVATION

A never-ending goal in the development of space satellites is increasing mass specific power while maintaining longevity. Therefore, it is important for the solar cell devices powering satellites to be both lightweight and tolerant to a degree of radiation. The main cause of solar cell degradation in space is due to high energy radiation effects that exist in the Van Allen belts where charge particles are trapped by the Earth's magnetic field. Atomic displacements that are created by high electron and proton fluxes as a result of solar winds are the major cause of degradation, and ultimately lead to reduced device performance over time. The need for power generation in space for satellites and space missions has historically led to a significant amount of research based on determining the effects of radiation damage on semiconductors in a space environment. Many techniques have been investigated to increase the radiation tolerance of photovoltaic devices, from simpler design changes such as device polarity and cover glass shielding [58] to changing to more radiation hard materials [59] to

moving to lattice-mismatched devices such as the inverted metamorphic (IMM) device, which takes advantage of inverted growth to yield a thin solar cell [33, 36, 60].

Thin solar cells have an immediate advantage in a space environment because they are lightweight. One method for processing thin devices is epitaxial lift-off which both eliminates substrate weight and allows for substrate reuse. This technique has even been extended to IMM devices, based on a triple junction InGaP/GaAs/InGaAs structure [34]. However, little research has been performed on the advantages with respect to radiation tolerance that thin devices have, such as those fabricated by epitaxial lift-off. In this study, a sample set of single junction baseline and quantum dot-enhanced GaAs solar cells discussed in Chapter 2 underwent alpha irradiation to gauge the radiation tolerance of these devices. Results will be discussed after an introduction to radioisotopes and effects of high-energy particle interaction with a semiconductor crystal lattice.

3.2 THEORY

3.2.1 Radioactive Isotopes

Radioactive isotopes, also known as radioisotopes, have unstable nuclei that results in spontaneous nuclear decays in the form of alpha (α) particles, beta (β) particles, or gamma (γ) rays. The rate of radioisotope decay is directly proportional to the number of radionuclides and the probability of decay, and can be used to describe the activity of the sample as a function of time. This formulation is given in Equation 3.1, where

N_0 is the initial number of radionuclides and λ is the probability of decay. A commonly used unit of activity is the curie (Ci), equal to 37 billion decays per second. Half-life is used to describe the lifetime of a radioisotope by its relation to decay probability, as shown in Equation 3.2.

$$A = N_0 \lambda e^{(-\lambda t)} = A_0 e^{(-\lambda t)} \tag{3.1}$$

$$t_{1/2} = \frac{ln(2)}{\lambda} \tag{3.2}$$

An α-particle is a high energy double-ionized helium nucleus consisting of two protons and two neutrons. An alpha decay results in an atom that has an atomic number reduced by two and atom weight reduced by four. A β-particle is a high energy electron created from neutron decay in a radioisotope. A beta decay results in an atom with an atomic number increased by one. A γ-ray is an emission of a high energy photon that can occur spontaneously or with alpha and beta radiation. Gamma rays result from energetic transitions of nuclei left in an excited state following radioactive decay. Since the diameter of an atom is much larger than the diameter of its nucleus, an electron collision is most probable.

3.2.2 Radiation Interaction With Semiconductors

A high energy particle will transfer some or all of its energy to a bonded atom when incident on a semiconductor lattice, and is back-scattered at some angle. Energy

losses are divided into two categories: ionizing and non-ionizing interactions. Ionizing energy loss occurs when the incident particle collides with a bound electron, forcing it out of position and ionizing the atom. Another electron can be captured by the ionized atom, neutralizing the charge. Non-ionizing energy loss (NIEL) occurs when a high-energy particle is incident on an atomic nucleus, which can move the atom from its position in the lattice, as shown in the schematic in Figure 3.1. The atom is termed the primary knock-on atom (PKO), which becomes displaced and can disrupt the periodicity of the lattice by creating a vacancy and an interstitial site along its path. In this situation the defect pair generated is known as a Frenkel defect. These defect pairs and other defect complexes can create localized energy states in the bandgap of the semiconductor, affecting charge transport through carrier generation, recombination, trapping, compensation, or trap-assisted tunneling [61].

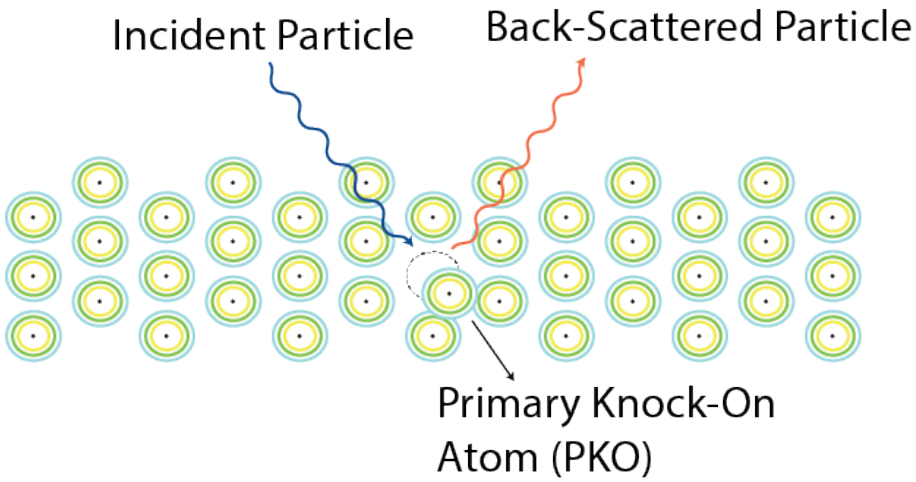

Figure 3.1: Atom displacement in a 2-d lattice due to radiation damage.

The NIEL of a material-particle system is related to the threshold energy for atomic displacement (E_{th}), as an increase in E_{th} means that a greater amount of energy

transferred to the PKO atom and subsequent collisions is required to generate a defect. The number of vacancies created will be decreased, and overall the material will appear more tolerant to radiation. It has been shown that strain induced by a QD superlattice has a significant impact on the value of E_{th} [62], and that whether the strain is of a compressive or tensile nature will affect device operation differently [39]. NIEL can be calculated using Equation 3.3, where N is Avogadro's number, A is the atomic mass, L is the Lindhard Partition factor (which gives the fraction of transferred energy that is nonionizing), T is the recoil energy of the target atoms, and $d\sigma/d\Omega$ is the differential scattering cross-section of atomic displacements. The lower integral limit, θ_{min}, is the scattering angle for which the recoil energy is equal to E_{th} [61, 63, 64]. An introduction of a quantity called the displacement damage dose is useful to compare radiation damage across different particles and particle energies, and can be used to predict radiation effects at an equivalent fluence. The displacement damage dose, D_d, is the amount of displacement damage energy imparted per unit material given in units of $\mathrm{MeV/g}$, and is the product of NIEL and the particle fluence.

$$NIEL(E) = \frac{N}{A}\int_{\theta_{min}}^{\pi}\Big(\frac{d\sigma(\theta,E)}{d\Omega}\Big)T(\theta,E)L[T(\theta,E)]d\Omega \tag{3.3}$$

More fundamentally, the main damage mechanism resulting from radiation is minority carrier diffusion length degradation due to radiation-induced defects that act as traps and recombination centers. This reduction in diffusion length lowers the quantum efficiency of a device because generated carriers are less likely to reach the junction. Since the base of a solar cell is typically much thicker than the emitter, degradation

is observed most in longer wavelength response. By determining the minority carrier diffusion length at various fluences, a damage coefficient K_L can be determined. Damage coefficients are a typical way to compare different types of radiation [65]. Damage to the lattice is concentrated near the stopping range of the particle, and increases carrier trapping and scattering events. K_L can be determined at a particle fluence using Equation 3.4, where L_0 is the initial diffusion length and L_ϕ is the degraded diffusion length.

$$\frac{1}{L_\phi^2} = \frac{1}{L_0^2} + K_L\phi \tag{3.4}$$

3.3 EXPERIMENTAL SET-UP

3.3.1 Testing Setup

In order to gauge the radiation tolerance of devices that have embedded QDs, a set of samples underwent a series of alpha radiation exposures. Although α-particles are not present in high fluxes in space, sources are easily available in the lab that are relatively safe because of their short penetration depth, on the order of the thickness of a sheet of paper or $40\,\mathrm{mm}$ in air. In addition, α-particles are energetic enough to cause the lattice dislocations that would be seen in a space environment. Compared to electron or proton radiation, alpha radiation is more harsh and may be more indicative of solar cells exposed to a nuclear blast.

The $4''$ wafers were diced prior to irradiation. This created some difficulty in getting

the individual devices flat during subsequent measurements, due to being very thin and of a small area. However, this did not seem to have an effect on series resistance measurements, although shunt resistance measurements varied by a few orders of magnitude. This may have also caused a non-uniform exposure during alpha irradiation, as the flux incident on a cell is emitted isotropically from the α source. The imparted damage will thus reduce with increasing depth into the cell and radial distance from the source. If the edges of the cells are curled up because the device is not perfectly flat, the damage around the cell may vary as well. To account for this, extra care was taken so that each individual measurement was consistent. Device performance characteristics under AM0 illumination were measured after each exposure using a dual source solar simulator from TS Space Systems, as discussed in the previous chapter. Spectral response measurements were taken with a Newport IQE 200 tool.

3.3.2 Alpha Particle Calibration and Setup

An in-house ^{210}Po radioisotope with an activity of $1\,\mathrm{mCi}$ was used as the alpha source. ^{210}Po has a half-life of 138.376 days and emits $5.4\,\mathrm{MeV}$ α particles. The flux of the ^{210}Po source was measured using a pinhole in parafilm and a geiger counter resting on the can, which is depicted in Figure 3.2. An acceptance angle of nearly π was assumed, since the geiger counter head was much larger than the pinhole. A background "baseline" γ ray measurement was required using an unbroken piece of parafilm in order to get an accurate reading of counts coming only through the pinhole.

No additional shielding of the α source was required because of the relatively low flux and the short penetration depth of the α particles. The flux of the α source was calculated to be $8.5 \times 10^6\,\alpha/\mathrm{cm}^2/\mathrm{s}$ just prior to the experiment. Single devices from baseline and QD ELO wafers were tested prior to and intermittently following increasing exposure levels. Exposure times were chosen to achieve doses varying in single orders of magnitude from $5 \times 10^7\,\alpha/\mathrm{cm}^2$-$5 \times 10^{10}\,\alpha/\mathrm{cm}^2$.

Figure 3.2: Can containing ^{210}Po source.

The non-ionizing energy loss (NIEL) for an omni-directional alpha source was calculated using the monte-carlo simulation software MCNPX. The calculation of displacement damage dose (D_d) from alpha fluence was completed according to the formulation developed by Summers [64], which has been shown to be an effective method to compare various types of radiation exposures. The D_d value was calculated for upright GaAs devices with a thick substrate, but is the same in this case for the thinner ELO device of a similar active thickness ($2.5 - 3.0\,\mu\mathrm{m}$). Using a D_d value of $0.125\,\mathrm{MeV/g/alpha}$ for GaAs, fluences were converted to a D_d range of $6.25 \times 10^6\,\mathrm{MeV/g}$ - $6.25 \times 10^9\,\mathrm{MeV/g}$.

3.4 RESULTS

3.4.1 Alpha Radiation

A series of alpha radiation exposures was investigated to compare the radiation tolerance of ELO devices with and without QDs. J-V and spectral response measurements were taken following each exposure. J-V plots under 1-sun AM0 conditions are shown in Figure 3.3. Solar cell metrics as a function of increasing α-particle fluence or calculated displacement damage dose lends a more insightful visual comparison between the baseline and QD ELO devices, and will be discussed later. It can be noted from Figure 3.3 that at lower fluences, the QD ELO cell appears to have a higher initial threshold for radiation effects, as the first two exposure curves lie almost on top of the curve from BOL. The QD device also has a smaller ΔV_{oc} than the baseline from BOL to a D_d value of $6.25 \times 10^9\,\mathrm{MeV/g}$ of around $110\,\mathrm{mV}$ compared to $150\,\mathrm{mV}$.

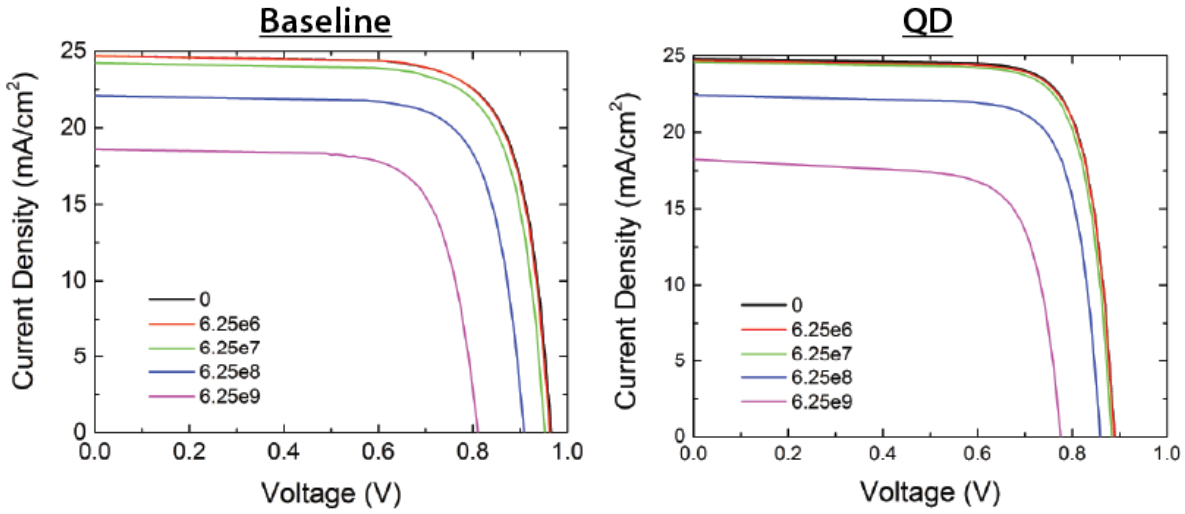

Figure 3.3: 1-sun AM0 J-V curves under increasing alpha radiation, given in displacement damage dose.

Spectral response measurements were taken at BOL and following the second exposure, and are shown in Figure 3.4. Clearly, much of the effects of radiation exposure led to a decrease in response in the base region of the device, corresponding to a reduction in the minority carrier diffusion length in the base. As the radiative particle imparts damage to the crystal lattice it generates defects, which increases the probability of carrier trapping and scattering. It is not until higher α fluences that a significant degradation in response is seen at shorter wavelengths. There was a larger degradation across all wavelengths observed in the QD cell at a D_d of $6.25 \times 10^9\,\mathrm{MeV/g}$. The MATLAB code described in the previous chapter was used to match the experimental EQE curves and extract diffusion length values for the emitter and base regions of the device. Figure 3.5(a) depicts extracted diffusion lengths in absolute values as a function of increasing dose, while Figure 3.5(b) shows these as normalized to the diffusion length values at BOL. The emitter diffusion lengths track similarly for baseline and QD ELO devices measured. While the QD cell sees a higher degradation initially in the base diffusion length, this reduction slows with increasing dose and tracks closely to the baseline cell.

The radiation hardness of the QD ELO cells when compared to the baseline ELO cells is further illustrated in Figure 3.6. Figure 3.6(a) depicts remaining solar cell figures of merit for J_{sc}, V_{oc}, and P_{max} for both QD and baseline ELO devices. Clearly, up to EOL the QD ELO cell outperforms the baseline ELO cell with a slower rate of decrease in J_{sc} and notably in V_{oc}. In addition, the absolute difference of FF/FF_0 results at EOL between QD and baseline samples was less than 1%. This leads to a

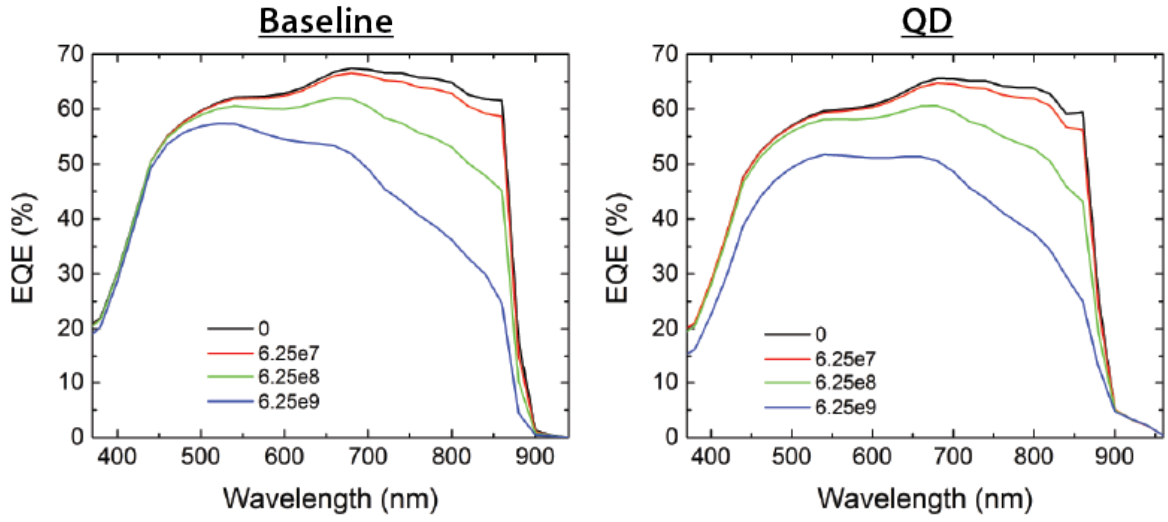

Figure 3.4: EQE curves for increasing displacement damage dose from alpha irradiation.

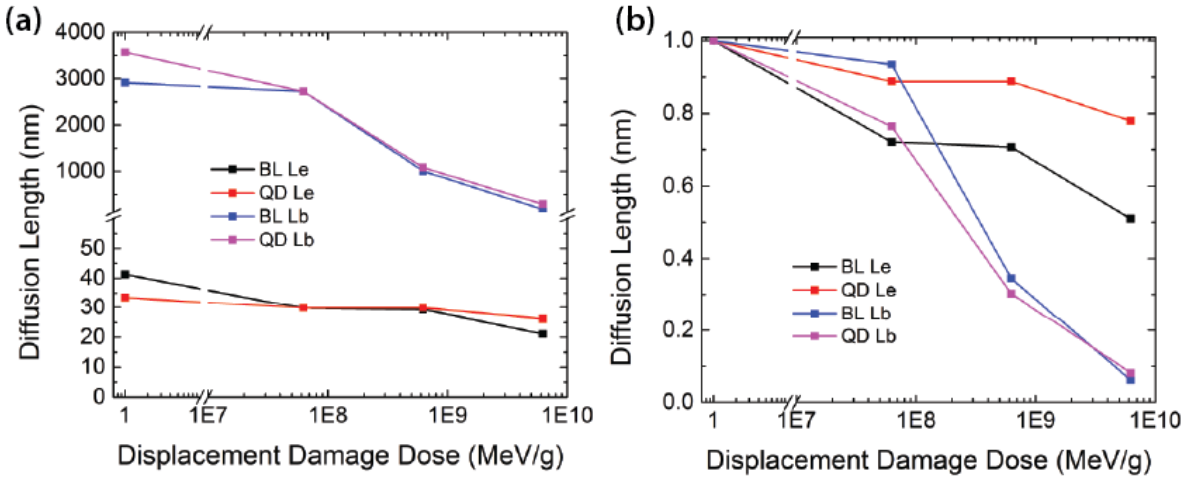

Figure 3.5: Diffusion length values extracted from MATLAB simulations as a function of displacement damage dose, given in absolute values (a) and as remaining factors of BOL (b).

higher η/η_0 remaining factor for the QD device with respect to the baseline up to a D_d of $6.25 \times 10^8\,\mathrm{MeV/g}$, corresponding to an alpha particle fluence of $5 \times 10^9\,\alpha/\mathrm{cm}^2/\mathrm{s}$.

Furthermore, the EQE curves in Figure 3.4 following each radiation exposure were used to compare the effect of bulk integrated J_{sc} values to sub-GaAs bandgap integrated J_{sc} values in order to further gauge the addition of QDs on cell performance.

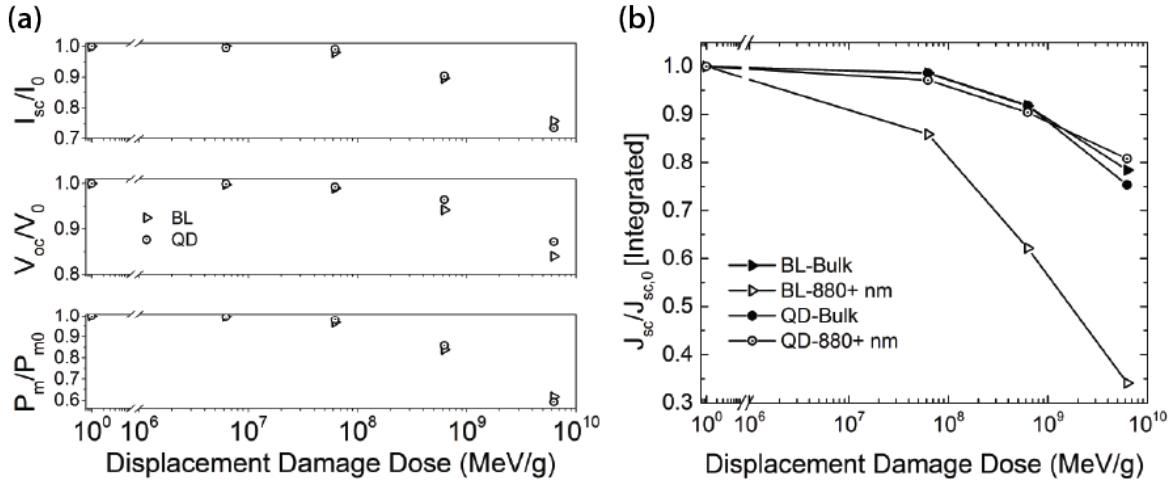

Figure 3.6: (a) Remaining factor solar cell metrics under alpha irradiation for baseline and QD ELO cells; (b) Remaining factor plot of integrated J_{sc} for both bulk wavelengths (300-880 nm) and sub-GaAs wavelengths (880-1050 nm) as a function of radiation displacement damage dose for baseline and QD cells. EOL is measured at $6 \times 10^8\,\mathrm{MeV/g}$.

Figure 3.6(b) shows integrated J_{sc} values obtained from the convolution of measured spectral response with the AM0 spectrum, as explained previously, as a function of displacement damage dose.

Clearly, there is a more consistent sub-GaAs bandedge integrated J_{sc} for samples with embedded QDs. At EOL, remaining factor for the QD cell is 0.90, and for the baseline cell is 0.62. After the GaAs band edge, collection is maintained at EOL relative to BOL. This may be due to residual compressive strain local to the QD region resulting in decreased probability for defect formation by increasing the barrier for a primary knock-on atom to reach an interstitial site, and has been previously observed in upright devices with 5 QD layers [62]. In addition, Figure 3.7, which shows EQE measurements for a QD ELO sample at both beginning of life (BOL) and EOL. It is

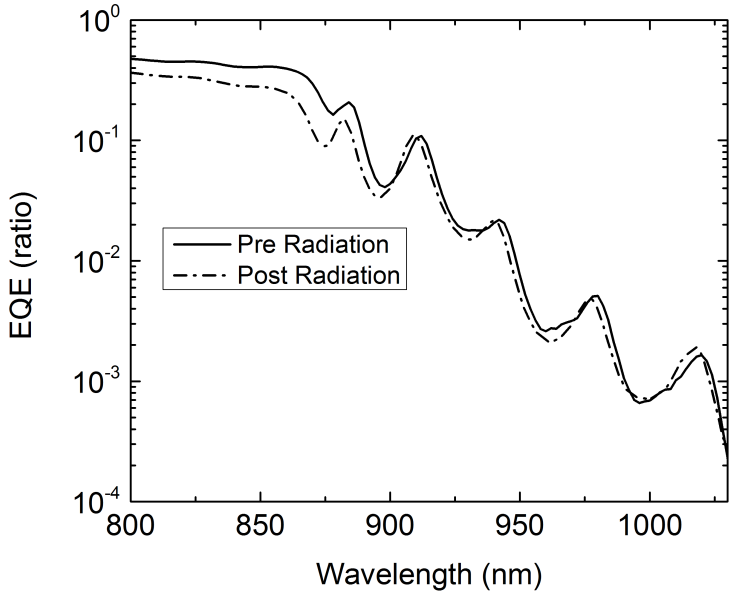

Figure 3.7: EQE curve of sub-GaAs wavelengths (880-1050 nm) of a QD cell device measured prior to and following alpha irradiation, at BOL and EOL.

evident that after $900\,\mathrm{nm}$ there is a negligible difference in the two curves, which indicates the QDs themselves are mainly unaffected by the radiation, or interact less with alpha particles due to occupying a smaller volume.

During the radiation study discussed in this chapter, temperature coefficients were measured using similar techniques as described in the previous chapter. The temperature study was completed in nominal temperature steps of $20\,^{\circ}\mathrm{C}$ from $20\,^{\circ}\mathrm{C}$ to $80\,^{\circ}\mathrm{C}$. Temperature coefficients for both the baseline and QD ELO samples were then calculated using linear fits for experimental AM0 1-sun J-V curves. Figure 3.8 plots each temperature coefficient for both the baseline and QD ELO samples together for ease in comparison of the effects of QD inclusion. At end of life, it is apparent that the QD device has better temperature coefficients for J_{sc} and V_{oc}. However, a downward-trending fill factor and V_{oc} temperature coefficient for the QD device leads to a slightly

higher η temperature coefficient for the baseline device.

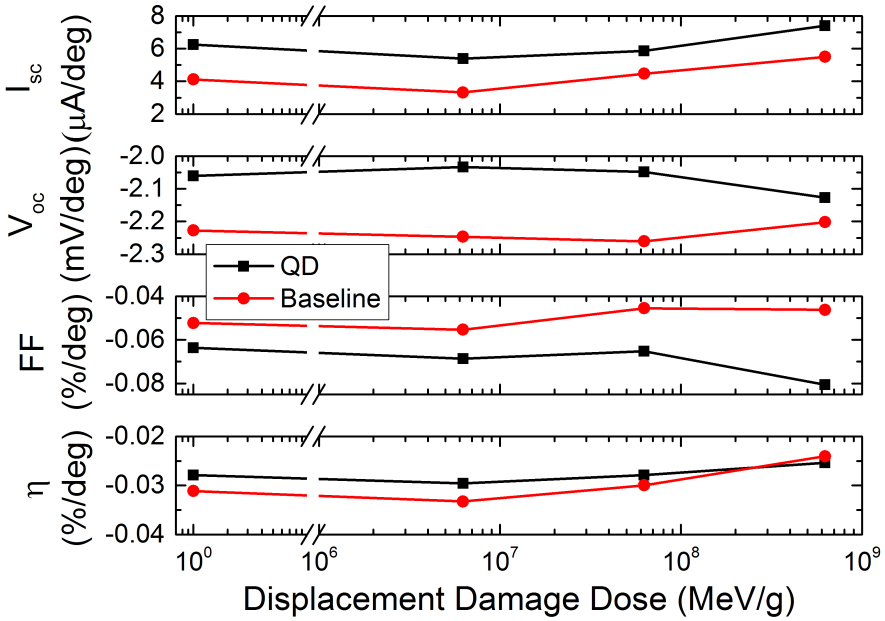

Figure 3.8: Temperature coefficients for I_{sc}, V_{oc}, FF, and η plotted as a function of displacement damage dose for both a baseline and QD ELO device.

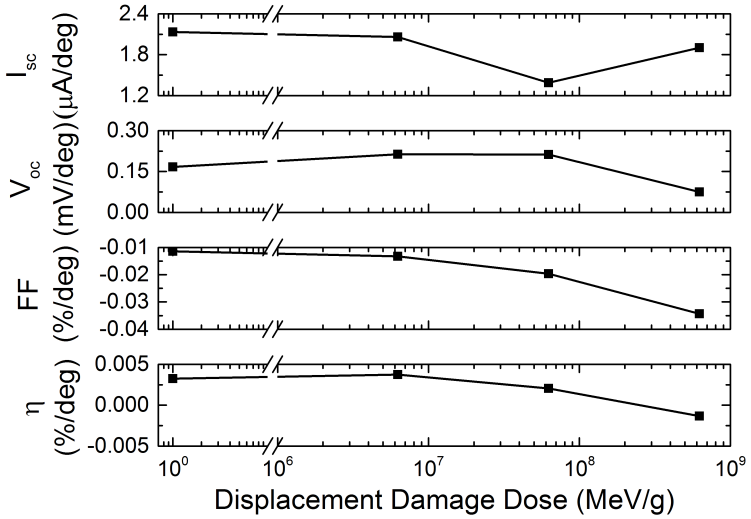

Figure 3.9: Difference in temperature coefficients for solar cell 1-sun figures of merit between the QD and baseline devices, shown as function of increasing displacement damage dose from α irradiation.

The trend changes between the QD and baseline devices are easily observed

when compared by the difference between the two, as in Figure 3.9. Clearly, the J_{sc} temperature coefficient is higher for the QD device. V_{oc} and FF temperature coefficients show similar trend shapes as they exhibit trends towards lower values following increasing dosage, although the temperature coefficient for V_{oc} is higher for the QD device while the FF temperature coefficient is smaller. The η temperature coefficient is higher for the QD device up to a D_d value of approximately $1 \times 10^8\,\mathrm{MeV/g}$, where the corresponding baseline temperature coefficient becomes higher. Devices in a space environment will need to withstand high-energy particle radiation and will also be subject to temperature extremes. At high doses of radiation corresponding to an EOL D_d of $6.25 \times 10^8\,\mathrm{MeV/g}$, the QD ELO device had a higher J_{sc} temperature coefficient, but faster degradation to V_{oc} led to a lower V_{oc} temperature coefficient, resulting in a lower conversion efficiency.

3.5 CONCLUSIONS

A series of alpha radiation exposures was investigated to compare the radiation tolerance of ELO devices with and without QDs. The QD devices outperform baseline devices with a remaining factor increase of 2% in conversion efficiency at an end of life alpha particle fluence of $5 \times 10^9\,\alpha/\mathrm{cm}^2/\mathrm{s}$, corresponding to a calculated displacement damage dose value of $6.25 \times 10^8\,\mathrm{MeV/g}$. The incident α-particles generate defects in the crystal lattice, which increases the probability of carrier trapping and scattering. This manifests as a drastic reduction in the minority carrier diffusion length in the base

at high fluences. The rate of this reduction in baseline and QD ELO devices is comparable based on modeling of experimentally measured EQE curves via drift-diffusion equations in MATLAB. However, QD solar cell figures of merit under 1-sun AM0 conditions are higher at EOL, particularly V_{oc}, J_{sc}, and P_{max}. The QD device has a smaller ΔV_{oc} than the baseline from BOL to a D_d value of $6.25 \times 10^9\,\mathrm{MeV/g}$ of around $110\,\mathrm{mV}$ compared to $150\,\mathrm{mV}$. Furthermore, the radiation study was expanded by taking J-V curves at several temperatures in order to extract temperature coefficients. The QD device exhibits better V_{oc} and J_{sc} temperature coefficients at EOL than the baseline device, which leads to an overall better performing device with a larger efficiency temperature coefficient. This is promising as it is advantageous for devices in solar orbits to be both lightweight and radiation hard.

Chapter 4

CONCLUSIONS AND FUTURE WORK

4.1 Conclusions

InAs/GaAs QD-ELO solar cells were grown and fabricated for the first time to yield thin solar cells with an increased collection and absorption in sub-GaAs bandgap wavelengths due to carrier absorption into QD states. Optical and materials characterization and analysis of test structures showed a successful ELO transfer with QD structures. These devices included 10 layers of QDs, which can be extended to increase the filling factor of the QD superlattice. Analysis of device characterization showed a higher short circuit current density for QD cells when compared to the baseline cell by an absolute value of $0.12\,\mathrm{mA/cm^2}$. In addition, integrated EQE past the GaAs bandedge quantified the QD contribution to the short circuit current density as $0.23\,\mathrm{mA/cm^2}$ due to QD photocurrent enhancement. Light trapping was an important factor in increasing the OPL of light through the superlattice, and can be optimized in

future work to increase the efficiency of these devices. Further efficiency enhancement is expected by optimizing the growth process and incorporating improved backside light management techniques to increase the optical path length of incoming IR light through the QDs. A highly reflective backside mirror could ideally improve reflectivity by almost 20%.

In addition, analysis of alpha radiation effects showed that the QD ELO cells have a better radiation hardness when compared to the baseline at an end-of-life alpha particle fluence of $5 \times 10^9\,\alpha/\mathrm{cm}^2/\mathrm{s}$, which corresponds to a calculated displacement damage dose value of $6.25 \times 10^8\,\mathrm{MeV/g}$. Furthermore, the QD ELO cell exhibited larger V_{oc} and J_{sc} temperature coefficients at end of life, which led to a higher η temperature coefficient up to a D_d value of approximately $1 \times 10^8\,\mathrm{MeV/g}$. Thin, flexible, and radiation hard solar cells are immensely advantageous in a space environment where the radiation effects of the Van Allen belts can affect cell performance over time, and where large temperature fluctuations occur daily. These QD ELO cells are promising candidates for development in a new ELO TJSC that could potentially outperform the current state-of-the-art space solar cell due to increased current, radiation hardness, and flexibility.

4.2 Future Work

4.2.1 Backside Reflector

As explained in previous sections, the optimization of a high-reflectance mirror on the backside of ELO wafers could significantly improve the observed sub-bandgap J_{sc} enhancement from QD states. As a preliminary step to gauge the effects of improving the reflectivity of the backside metal, $2''$ upright wafers were grown using MOVPE on (100) substrates misaligned 2° to the [110]. A single side polished (SSP) and a double side polished (DSP) wafer, each with a 10-layer QD superlattice, were grown and compared to a baseline (BL) solar cell with no QDs. Zn and Si were used as p- and n- type dopants, respectively. The wafers were processed in the RIT Semiconductor Manufacturing and Fabrication Laboratory (SMFL). Both wafers had seven $1\text{x}1\,\mathrm{cm}^2$ cells defined lithographically on the front side of the wafer, along with several test structures.

The wafers were fabricated using standard III-V techniques for lithography and layer etching. General process flow involved backside metallization, annealing of backside contact, frontside metallization, MESA isolation etch, contact layer removal, and annealing of frontside contacts. Heavily doped layers were used as semiconductor contacts. A lift-off process with a bi-layer resist was used to pattern the frontside devices. $Au/Zn/Au$ p-type metal contacts were thermally evaporated onto the front, and $Ge/Au/Ni/Au$ n-type metal contacts to the backside. The layer structure is shown in Figure 4.1.

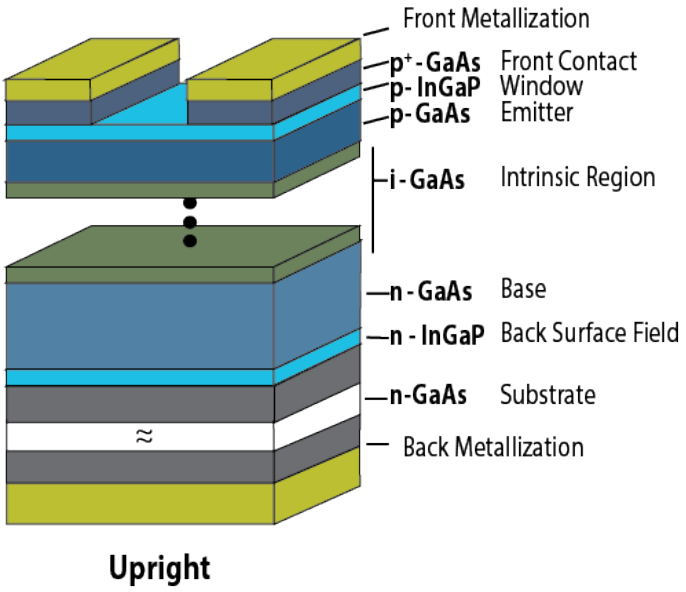

Figure 4.1: Upright solar cell structure detailing compounds used in the layer stack.

The DSP sample was put through an initial processing step to deposit a thin layer of approximately $160\,\mathrm{nm}$ of SiO_2 on the backside using PECVD. This thickness was chosen based on MATLAB simulations shown in Figure 4.2. The simulation was run to determine the optimum thickness for the dielectric layer that would allow for maximum reflection, as well as show the allowable amount of uncertainty in the deposition process. The simulation iteratively found the optimum SiO_2 thickness based on separately maximizing reflectivity as well as current density generated under AM1.5 illumination. Additional simulations could be performed to optimize the reflectivity with a stack including a thin back surface field layer.

An array of via holes was patterned lithographically through the SiO_2 to serve as a contact from the metal to the underlying GaAs layer, as depicted in Figure 4.3(a). This processing step was completed first, prior to backside metallization. $Ge/Au/Ni/Au$ thermally evaporated contacts were selectively deposited in the via holes, and then

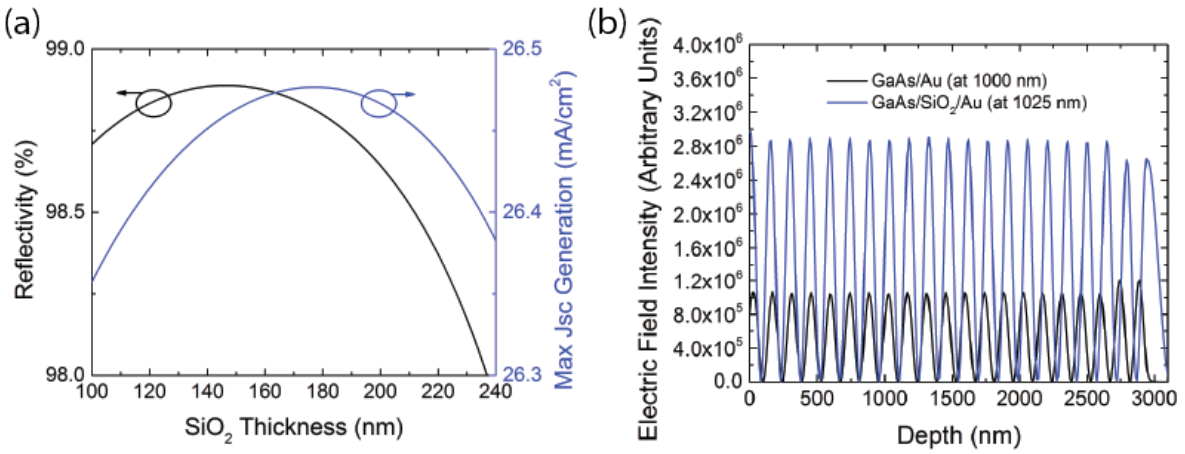

Figure 4.2: (a) Simulation performed using MATLAB that optimized SiO_2 thickness layer based on maximizing reflectivity and current density; (b) FDTD simulation for a structure with and without SiO_2 grading. Note that the electric field intensity is maximized at a different wavelength.

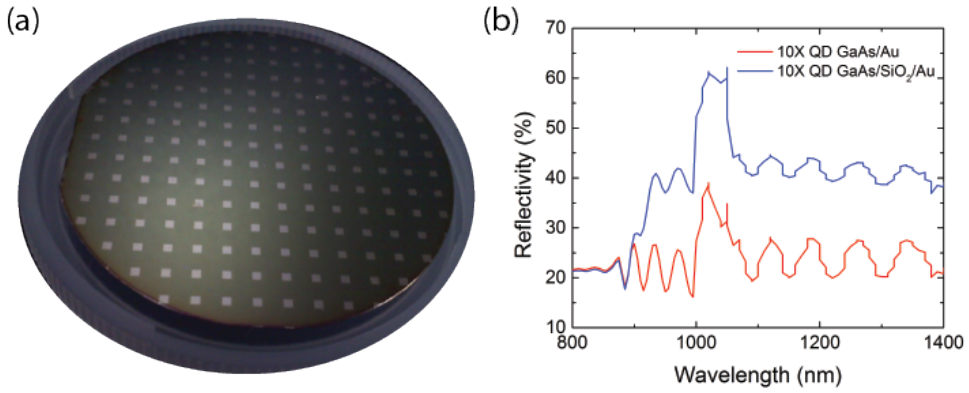

Figure 4.3: (a) Patterned back surface of a 2″ GaAs QDSC for electrical contact; (b) experimental reflectivity measured for a 10x QD device with and without the SiO_2 dielectric layer included.

the entire backside was coated with Au for reflectivity. The SiO_2 layer was used as a dielectric grading to enhance the optical interface between GaAs and a gold (Au) metallic reflector, and as depicted in Figure 4.3(b) dramatically increases the reflectivity past $900\,\mathrm{nm}$. The via lithography mask consisted of a 31x31 array of 1x$1\,\mathrm{mm}^2$ holes spaced $0.23\,\mathrm{cm}$ apart, allowing for approximately 10% coverage of the total back

surface area. The GaAs/SiO_2/Au stack serves as a backside reflector to allow for multiple passes of infrared light through the QD layer, and is hypothesized to act as a substitute for growing thicker stacks of QDs. Figure 4.4 shows experimental results for 1-sun AM0 J-V curves and EQE calculated from spectral response, and the results are summarized in Table 4.1. Even with a thick substrate, the QD cell receives benefits from the inclusion of the SiO_2 layer, resulting in a V_{oc} increase as well as a subband current enhancement. This can be increased further by combining such a reflector with a QDSC processed by ELO.

Table 4.1: 1-Sun AM0 Upright Device J-V And Integrated Spectral Response Results

	J_{sc} $(\mathrm{mA/cm^2})$	V_{oc} (V)	FF $(\%)$	η $(\%)$	J_{SR} Bulk $(\mathrm{mA/cm^2})$	J_{SR}, $\lambda > 880\,\mathrm{nm}$ $(\mathrm{mA/cm^2})$
Baseline	23.7	1.06	82	14.5	23.5	0.022
10X QD (no reflector)	23.1	0.87	73	10.8	23.9	0.199
10X QD (with reflector)	22.9	0.88	75	11.1	23.8	0.237

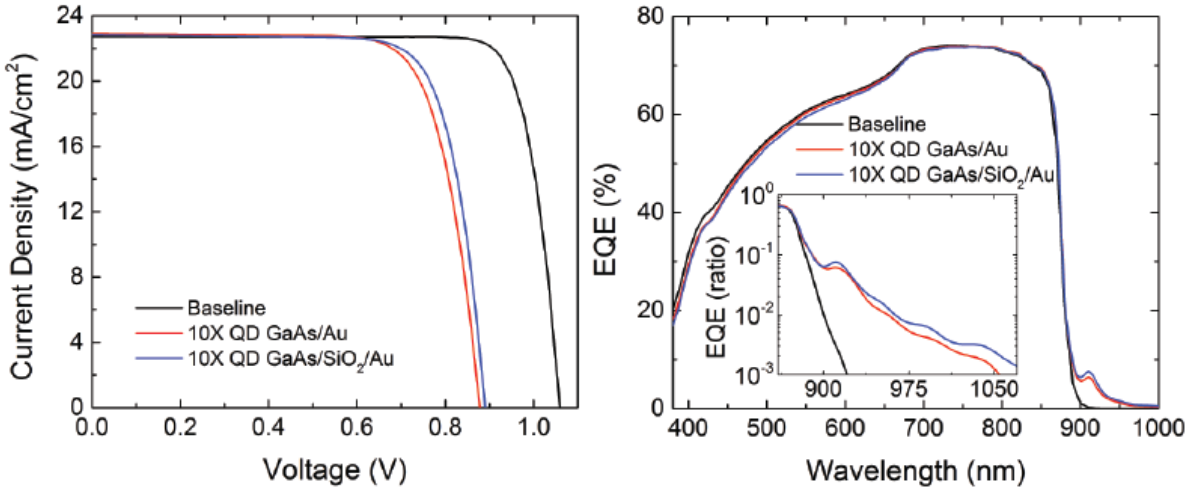

Figure 4.4: 1-sun AM0 J-V curves (left) and EQE spectra (right) for upright 2″ devices.

References

[1] G. W. Crabtree and N. S. Lewis, “Solar energy conversion,” Physics Today, 2008.

[2] E. Gaddy, R. Decker, M. Lockwood, L. Roufberg, G. Knutzen, and D. Marsh, “The solar probe plus solar array development and design,” in 35th IEEE Photovoltaic Specialists Conference, 2010.

[3] W. Shockley and H. J. Queisser, “Detailed balance limit of efficiency of p-n junction solar cells,” Journal of Applied Physics, vol. 32, no. 3, 1961.

[4] L. C. Hirst and N. J. Ekins-Daukes, “Quantifying intrinsic loss mechanisms in solar cells: Why is power efficiency fundamentally limited?,” in Proceedings of SPIE, 2010.

[5] R. Oshima, H. Komiyama, T. Hashimoto, H. Shigekawa, and Y. Okada, “Fabrication of multi-layer self-assembled InAs quantum dots for high-efficiency solar cells,” in 4th IEEE World Conference on Photovoltaic Energy Conversion, 2006.

[6] R. Oshima, A. Takata, and Y. Okada, “Strain-compensated InAs/GaNAs quantum dots for use in high-efficiency solar cells,” Applied Physics Letters, vol. 93, no. 8, 2008.

[7] S. M. Hubbard, C. D. Cress, C. G. Bailey, R. P. Raffaelle, S. G. Bailey, and D. M. Wilt, “Effect of strain compensation on quantum dot enhanced GaAs solar cells,” Applied Physics Letters, vol. 92, no. 12, 2008.

[8] J. Liang and Z. Suo, “Stable island arrays by height-constrained Stranski-Krastanov growth,” Applied Physics Letters, vol. 79, no. 20, 2001.

[9] R. Muhammad, Z. Othaman, L. K. Boo, and Y. Wahab, “InAs/GaAs quantum dots grown by metal organic chemical vapor deposition at different temperatures,” Modern Applied Science, vol. 2, no. 3, 2008.

[10] A. A. El-Emawy, S. Birudavolu, P. S. Wong, Y.-B. Jiang, H. Xu, S. Huang, and D. L. Huffaker, “Formation trends in quantum dot growth using metalorganic chemical vapor deposition,” Journal of Applied Physics, vol. 93, no. 6, 2003.

[11] H. S. Lee, J. Y. Lee, T. W. Kim, and M. D. Kim, “Strain effects in and crystal structures of self-assembled InAs/GaAs quantum dots,” Applied Physics Letters, vol. 83, no. 11, 2003.

[12] A. Luque and A. Martí, “Increasing the efficiency of ideal solar cells by photon induced transitions at intermediate levels,” Physical Review Letters, vol. 78, no. 26, 1997.

[13] K. Yoshida and Y. Okada, “Device simulation of intermediate band solar cells,” in 12th International Conference on Numerical Simulation of Optoelectronic Devices (NUSOD), 2012.

[14] A. Martí, E. Antolín, C. Stanley, C. Farmer, N. López, P. Díaz, E. Cánovas, P. Linares, and A. Luque, “Production of photocurrent due to intermediate-to-conduction-band transitions: A demonstration of a key operating principle of the intermediate-band solar cell,” Physical Review Letters, vol. 97, no. 24, 2006.

[15] A. Luque, A. Martí, and C. Stanley, “Understanding intermediate-band solar cells,” Nature Photonics, vol. 6, no. 3, 2012.

[16] R. Strandberg and T. W. Reenaas, “Photofilling of intermediate bands,” Journal of Applied Physics, vol. 105, no. 12, 2009.

[17] Y. Okada, T. Morioka, K. Yoshida, R. Oshima, Y. Shoji, T. Inoue, and T. Kita, “Increase in photocurrent by optical transitions via intermediate quantum states in direct-doped InAs/GaNAs strain-compensated quantum dot solar cell,” Journal of Applied Physics, vol. 109, no. 2, 2011.

[18] N. López, A. Martí, A. Luque, C. Stanley, C. Farmer, and P. Díaz, “Experimental analysis of the operation of quantum dot intermediate band solar cells,” Journal of Solar Energy Engineering, vol. 129, no. 3, 2006.

[19] M. R. Khan, X. Wang, and M. A. Alam, “Fundamentals of PV efficiency: Limits for light absorption,” arXiv:1212.2897, 2012.

[20] H. A. Atwater and A. Polman, “Plasmonics for improved photovoltaic devices,” Nature Materials, vol. 9, no. 3, 2010.

[21] G. Lush and M. Lundstrom, “Thin film approaches for high-efficiency III-V cells,” Solar Cells, vol. 30, no. 1-4, 1991.

[22] O. D. Miller, E. Yablonovitch, and S. R. Kurtz, "Intense internal and external fluorescence as solar cells approach the shockley-queisser efficiency limit," arXiv:1106.1603, 2011.

[23] G. Bauhuis, P. Mulder, E. Haverkamp, J. Huijben, and J. Schermer, "26.1% thin-film GaAs solar cell using epitaxial lift-off," Solar Energy Materials and Solar Cells, vol. 93, no. 9, 2009.

[24] B. M. Kayes, H. Nie, R. Twist, S. G. Spruytte, F. Reinhardt, I. C. Kizilyalli, and G. S. Higashi, "27.6% conversion efficiency, a new record for single-junction solar cells under 1 sun illumination," in 37th IEEE Photovoltaic Specialists Conference, 2011.

[25] R. Tatavarti, G. Hillier, A. Dzankovic, G. Martin, F. Tuminello, R. Navaratnarajah, G. Du, D. P. Vu, and N. Pan, "Lightweight, low cost GaAs solar cells on 4" epitaxial liftoff (ELO) wafers," in 33rd IEEE Photovoltaic Specialists Conference, 2008.

[26] R. Tatavarti, A. Wibowo, G. Martin, F. Tuminello, C. Youtsey, G. Hillier, N. Pan, M. W. Wanlass, and M. Romero, "InGaP/GaAs/InGaAs inverted metamorphic (IMM) solar cells on $4''$ epitaxial lifted off (ELO) wafers," in 35th IEEE Photovoltaic Specialists Conference, 2010.

[27] J. Adams, V. Elarde, A. Hains, C. Stender, F. Tuminello, C. Youtsey, A. Wibowo, and M. Osowski, "Demonstration of multiple substrate reuses for inverted metamorphic solar cells," IEEE Journal of Photovoltaics, vol. 3, no. 2, 2013.

[28] A. van Geelen, P. Hageman, G. Bauhuis, P. van Rijsingen, P. Schmidt, and L. Giling, "Epitaxial lift-off GaAs solar cell from a reusable GaAs substrate," Materials Science and Engineering: B, vol. 45, no. 1-3, 1997.

[29] J. Schermer, G. Bauhuis, P. Mulder, E. Haverkamp, J. van Deelen, A. van Niftrik, and P. Larsen, "Photon confinement in high-efficiency, thin-film III-V solar cells obtained by epitaxial lift-off," Thin Solid Films, vol. 511-512, 2006.

[30] H. Feng Lu, S. Mokkapati, L. Fu, G. Jolley, H. Hoe Tan, and C. Jagadish, "Plasmonic quantum dot solar cells for enhanced infrared response," Applied Physics Letters, vol. 100, no. 10, 2012.

[31] K. Tanabe, K. Watanabe, and Y. Arakawa, "Flexible thin-film InAs/GaAs quantum dot solar cells," Applied Physics Letters, vol. 100, no. 19, 2012.

[32] M. Stan, D. Aiken, B. Cho, A. Cornfeld, J. Diaz, V. Ley, A. Korostyshevsky, P. Patel, P. Sharps, and T. Varghese, "Very high efficiency triple junction solar cells grown by MOVPE," Journal of Crystal Growth, vol. 310, no. 23, 2008.

[33] J. F. Geisz, D. J. Friedman, J. S. Ward, A. Duda, W. J. Olavarria, T. E. Moriarty, J. T. Kiehl, M. J. Romero, A. G. Norman, and K. M. Jones, "40.8% efficient inverted triple-junction solar cell with two independently metamorphic junctions," Applied Physics Letters, vol. 93, no. 12, 2008.

[34] R. Tatavarti, A. Wibowo, V. Elarde, F. Tuminello, R. Pastor, T. Giannopoulos, M. Osowski, R. Chan, C. Youtsey, and G. Hillier, "Large-area, epitaxial lift-off, inverted metamorphic solar cells," in 37th IEEE Photovoltaic Specialists Conference, 2011.

[35] D. Wilt, S. Messenger, and A. Howard, "Technology opportunities to enable high mass specific power," in 34th IEEE Photovoltaic Specialists Conference, 2009.

[36] P. Patel, D. Aiken, A. Boca, B. Cho, D. Chumney, M. B. Clevenger, A. Cornfeld, N. Fatemi, Y. Lin, J. McCarty, F. Newman, P. Sharps, J. Spann, M. Stan, J. Steinfeldt, C. Strautin, and T. Varghese, "Experimental results from performance improvement and radiation hardening of inverted metamorphic multijunction solar cells," IEEE Journal of Photovoltaics, vol. 2, no. 3, 2012.

[37] S. M. Hubbard, C. Bailey, S. Polly, C. Cress, J. Andersen, D. Forbes, and R. Raffaelle, "Nanostructured photovoltaics for space power," Journal of Nanophotonics, vol. 3, no. 1, 2009.

[38] R. Leon, S. Marcinkecius, J. Siegert, B. Cechavicius, B. Magness, W. Taylor, and C. Lobo, "Effects of proton irradiation on luminescence emission and carrier dynamics of self-assembled III-V quantum dots," IEEE Transactions on Nuclear Science, vol. 49, no. 6, 2002.

[39] C. Kerestes, D. Forbes, Z. Bittner, S. Polly, Y. Lin, B. Richards, P. Sharps, and S. Hubbard, "Strain effects on radiation tolerance of quantum dot solar cells," in 38th IEEE Photovoltaic Specialists Conference, 2012.

[40] C. G. Bailey, D. V. Forbes, S. J. Polly, Z. S. Bittner, Y. Dai, C. Mackos, R. P. Raffaelle, and S. M. Hubbard, "Open-circuit voltage improvement of InAs/GaAs quantum-dot solar cells using reduced InAs coverage," IEEE Journal of Photovoltaics, vol. 2, no. 3, 2012.

[41] C. G. Bailey, S. M. Hubbard, D. V. Forbes, and R. P. Raffaelle, “Evaluation of strain balancing layer thickness for InAs/GaAs quantum dot arrays using high resolution x-ray diffraction and photoluminescence,” Applied Physics Letters, vol. 95, no. 20, 2009.

[42] Image Metrology Scanning Probe Image Processor, url: http://www.imagemet.com/.

[43] S. Bailey, D. Snyder, P. Jenkins, D. Scheiman, R. Mueller, V. Pichetto, K. Emery, C. Baur, S. Messenger, and C. Goodbody, “Standards for space solar cells and arrays,” in 7th European Space Power Conference, 2005.

[44] H. Hovel and J. Woodall, “Theoretical and experimental evaluations of gaalas - gaas solar cells,” in Proceedings of the IEEE Photovoltaic Specialists Conference, 1973.

[45] S. M. Hubbard, A. Podell, C. Mackos, S. Polly, C. G. Bailey, and D. V. Forbes, “Effect of vicinal substrates on the growth and device performance of quantum dot solar cells,” Solar Energy Materials and Solar Cells, vol. 108, 2013.

[46] S. Hubbard, D. Wilt, S. Bailey, D. Byrnes, and R. Raffaelle, “OMVPE grown InAs quantum dots for application in nanostructured photovoltaics,” in 4th IEEE World Conference on Photovoltaic Energy Conversion, 2006.

[47] O. Stier, M. Grundmann, and D. Bimberg, “Electronic and optical properties of strained quantum dots modeled by 8-band k*p theory,” Physical Review B, vol. 59, no. 8, 1999.

[48] J. M. Gérard, B. Sermage, B. Gayral, B. Legrand, E. Costard, and V. Thierry-Mieg, “Enhanced spontaneous emission by quantum boxes in a monolithic optical microcavity,” Physical Review Letters, vol. 81, no. 5, 1998.

[49] M. Ohring, “Deposition and structure,” in Materials Science Of Thin Films, Academic Press, 2002.

[50] ImageJ: Image Processing and Analysis in Java, url: http://rsbweb.nih.gov/ij/.

[51] C. Cress, S. Hubbard, S. I. Maximenko, C. Bailey, D. Forbes, R. Raffaelle, M. Twigg, and R. Walters, “Analysis of strain compensated GaAs-based InAs QD solar cells,” in 34th IEEE Photovoltaic Specialists Conference, 2009.

[52] K. Sears, J. Wong-Leung, H. H. Tan, and C. Jagadish, “A transmission electron microscopy study of defects formed through the capping layer of self-assembled InAsGaAs quantum dot samples,” Journal of Applied Physics, vol. 99, no. 11, 2006.

[53] D. Bimberg, M. Grundmann, and N. N. Ledentsov, Quantum Dot Heterostructures. Wiley, 1999.

[54] Y. Shoji, K. Akimoto, and Y. Okada, “Self-organized InGaAs/GaAs quantum dot arrays for use in high-efficiency intermediate-band solar cells,” Journal of Physics D: Applied Physics, vol. 46, no. 2, 2013.

[55] C. G. Bailey, D. V. Forbes, R. P. Raffaelle, and S. M. Hubbard, “Near 1 v open circuit voltage InAs/GaAs quantum dot solar cells,” Applied Physics Letters, vol. 98, no. 16, 2011.

[56] E. Antolín, A. Martí, C. D. Farmer, P. G. Linares, E. Hernández, A. M. Sánchez, T. Ben, S. I. Molina, C. R. Stanley, and A. Luque, “Reducing carrier escape in the InAs/GaAs quantum dot intermediate band solar cell,” Journal of Applied Physics, vol. 108, no. 6, 2010.

[57] J. Gardner, E. Albers, C. Bailey, S. Hubbard, and R. Raffaelle, “Thermal and spectroscopic characterization of quantum dot-enhanced solar cells,” in 34th IEEE Photovoltaic Specialists Conference, 2009.

[58] F. Smits, “The degradation of solar cells under van allen radiation,” IEEE Transactions on Nuclear Science, vol. 10, no. 1, 1963.

[59] R. J. Walters, S. R. Messenger, G. P. Summers, M. J. Romero, M. M. Al-Jassim, D. Arajo, and R. Garcia, “Radiation response of n-type base InP solar cells,” Journal of Applied Physics, vol. 90, no. 7, 2001.

[60] J. Boisvert, D. Law, R. King, D. Bhusari, X. Liu, A. Zakaria, W. Hong, S. Mesropian, D. Larrabee, R. Woo, A. Boca, K. Edmondson, D. Krut, D. Peterson, K. Rouhani, B. Benedikt, and N. H. Karam, “Development of advanced space solar cells at spectrolab,” in 35th IEEE Photovoltaic Specialists Conference, 2010.

[61] R. J. Walters, S. Messenger, J. H. Warner, C. D. Cress, M. Gonzalez, and S. Maximenko, “Modeling of radiation induced defects in space solar cells,” in 37th IEEE Photovoltaic Specialists Conference, 2011.

[62] C. Cress, C. G. Bailey, S. Hubbard, D. Wilt, S. G. Bailey, and R. Raffaelle, “Radiation effects on strain compensated quantum dot solar cells,” in 33rd IEEE Photovoltaic Specialists Conference, 2008.

[63] E. Burke, “Energy dependence of proton-induced displacement damage in silicon,” IEEE Transactions on Nuclear Science, vol. 33, no. 6, 1986.

[64] G. P. Summers, E. A. Burke, and M. A. Xapsos, “Displacement damage analogs to ionizing radiation effects,” Radiation measurements, vol. 24, no. 1, 1995.

[65] R. Walters, J. Warner, G. Summers, S. Messenger, and J. Lorentzen, “Radiation response mechanisms in multijunction III-V space solar cells,” in 31st IEEE Photovoltaic Specialists Conference, 2005.

[66] C. D. Cress, S. M. Hubbard, B. J. Landi, R. P. Raffaelle, and D. M. Wilt, “Quantum dot solar cell tolerance to alpha-particle irradiation,” Applied Physics Letters, vol. 91, no. 18, 2007.